

EVIDENCE THAT 50% OF BALQSO OUTFLOWS ARE SITUATED AT LEAST 100 PC FROM THE CENTRAL SOURCE

NAHUM ARAV^{1,†}, GUILIN LIU¹, XINFENG XU¹, JAMES STIDHAM¹, CHRIS BENN² AND CARTER CHAMBERLAIN¹

¹Department of Physics, Virginia Tech, Blacksburg, VA 24061, USA and
²Isaac Newton Group, Apartado 321, E-38700 Santa Cruz de La Palma, Spain

Draft version May 8, 2018

ABSTRACT

The most robust way for determining the distance of quasar absorption outflows is the use of troughs from ionic excited states. The column density ratio between the excited and resonance states yields the outflow number density. Combined with a knowledge of the outflow's ionization parameter, a distance from the central source (R) can be determined. Here we report results from two surveys targeting outflows that show troughs from SIV. One survey includes 1091 SDSS and BOSS quasar spectra, and the other includes higher-quality spectra of 13 quasars observed with the Very Large Telescope. Our SIV samples include 38 broad absorption line (BAL) outflows, and four mini-BAL outflows. The SIV is formed in the same physical region of the outflow as the canonical outflow-identifying species CIV. Our results show that SIV absorption is only detected in 25% of CIV BAL outflows. The smaller detection fraction is due to the higher total column density (N_H) needed to detect SIV absorption. Since R empirically anti-correlates with N_H the results of these surveys can be extrapolated to CIV quasar outflows with lower N_H as well. We find that at least 50% of quasar outflows are at distances larger than 100 pc from the central source, and at least 12% are at distances larger than 1000 pc. These results have profound implications to the study of the origin and acceleration mechanism of quasar outflows and their effects on the host galaxy.

Keywords: quasars: general — quasars: absorption lines

1. INTRODUCTION

Roughly one-third of observed quasars show outflows as blueshifted absorption troughs with respect to the active galactic nucleus (AGN) rest-frame spectrum (Hewett & Foltz 2003; Dai et al. 2008, 2012; Ganguly & Brotherton 2008; Knigge et al. 2008). Theoretical modeling has shown that such outflows can be a main agent of the so-called quasar-phase AGN feedback (e.g. Ostriker et al. 2010; Ciotti et al. 2010; Soker 2010; McCarthy et al. 2010; Hopkins & Elvis 2010; Faucher-Giguère et al. 2012; Choi et al. 2014). However, in order to gain insight on the nature of these outflows and their influence on the host galaxy, it is critical to constrain their distance from the central source (R). For example, most theoretical models predict that luminous quasars' outflows are accretion disk winds, which are observed in their acceleration phase at $R \sim 0.01$ pc (e.g. Murray et al. 1995; Elvis 2000; Proga et al. 2000, see § 7.3 for elaboration).

The most reliable observational method for determining R in AGN absorption outflows relies on measuring troughs from excited states of various ions. In § 2 we describe this method in detail, and in § 7 we compare this method with other empirical methods for determining R . Using the excited-state method over the last decade, our group and others measured R for about 20 AGN outflows, as well as their mass flow rate and kinetic luminosity (Hamann et al. 2001; de Kool et al. 2001, 2002a,b; Gabel et al. 2005; Moe et al. 2009; Bautista et al. 2010; Dunn et al. 2010; Aoki et al. 2011; Arav et al. 2012; Borguet et al. 2012a,b, 2013; Edmonds et al. 2011;

Arav et al. 2013; Lucy et al. 2014; Finn et al. 2014; Chamberlain et al. 2015a; Chamberlain & Arav 2015b). All of these investigations located the outflows at R of several pc to many kpc. For luminous quasars, the majority of these findings were at R of hundreds to thousands of pc scales (see Arav et al. 2013 for a review).

The majority of the R determinations referenced above arise from singly ionized species (e.g., Fe II and Si II). However, most outflows show absorption troughs only from more highly ionized species. Therefore, the applicability of R derived from singly ionized species to the majority of outflows is somewhat model-dependent (see discussion in § 1 of Dunn et al. 2012). To address this issue, several R determinations were done using doubly and triply ionized species. Three of these studies used HST to observe transitions from excited states shortward of 1000Å. These published results all found $R > 500$ pc (3000 pc using O IV and O IV*, Arav et al. 2013; 4000 pc using O IV and O IV*, Finn et al. 2014; 800 pc using N III and N III* Chamberlain & Arav 2015b), strongly suggestive of a large size scale for quasar outflows. However, the paucity of HST observations does not allow for a robust statistical conclusion regarding the distribution of R values.

In contrast, ground-based observations have provided many thousands of spectra of quasar outflows. From the ground, the main high-ionization species with a measurable trough arising from an excited state is SIV, which has resonance and excited level transitions at 1063 and 1072Å, respectively (see § 2). It is difficult to obtain high-quality spectra of similar diagnostics shortward of 1000Å, from the ground, due to the strongly increasing density of the Ly α forest at the redshifts needed to cover this spectral band. Therefore, R determina-

[†] Email: arav@vt.edu

tions for high-luminosity quasars, using high-ionization diagnostics from the ground, concentrated on using the above SIV diagnostics. Four such analyses are found in the literature. In three of these, SIV yielded the following distances: $R > 3000$ pc (Borguet et al. 2013), $R = 300$ pc (Borguet et al. 2013), and $R = 100$ pc (Chamberlain et al. 2015a). In one outflow, the SIV diagnostics could not provide an accurate constraint, but by using CIII* diagnostics, a distance range of $10 \text{ pc} < R < 300 \text{ pc}$ was established (Borguet et al. 2013).

However, analysis of individual objects suffers from selection biases. In order to establish the distribution of R in the general population of quasar outflows using the SIV diagnostics, we need to analyze unbiased samples — unbiased in the sense that the depth ratio of the SIV and SIV* troughs is not known a priori (see elaboration in § 2). In this paper, we present the analysis results of two such samples. The first is comprised of 1091 SDSS quasar spectra, and the second contains a blind sample of 13 outflows obtained with the Very Large Telescope (VLT) X-shooter spectrograph that have much higher data quality than the SDSS observations.

This paper is organized as follows. In § 2, we describe the physics and observational framework that allow us to use the SIV troughs to determine R . In § 3, we describe the samples selection, and in § 4, we describe the process of identifying and measuring the SIV and SIV* troughs. We present our results in § 5. In § 6 we detail the steps and assumptions that are needed to extrapolate these results to the general population of high ionization BALs (HiBAL) outflows. In § 7, we discuss these results, including their extrapolation for general broad absorption line (BAL) outflows, and show that the criticism about using the SIV diagnostics for R determination (Lucy et al. 2014) is unwarranted. We summarize this work in § 8.

2. USING SIV AND SIV* TROUGHS TO MEASURE DISTANCES OF AGN OUTFLOWS

As discussed in Borguet et al. (2012b), the SIV multiplet around 1070\AA is composed of three lines: the ground-state transition with a wavelength of 1062.66\AA , and two transitions arising from an excited state ($E = 951 \text{ cm}^{-1}$, hereafter, referred to as SIV*) at wavelengths 1072.96\AA and 1073.51\AA where the excited state being populated at a critical density of $n_{\text{cr}} = 5.6 \times 10^4 \text{ cm}^{-3}$ (at $10,000 \text{ K}$). Due to their small separation, for most applications we combine the excited 1072.96\AA and 1073.51\AA transitions to one transition (but see important exception in Borguet et al. 2012b, where the two excited-state troughs are somewhat resolved). The oscillator strength (f) of the combined excited transitions is equal to the $f = 0.05$ of the 1062.66\AA resonance transition (Verner et al. 1996). In passing, we mention that due to the same number of electrons in the outer shell, the following ions have a similar multiplet transition configuration that can also be used to extract measurements of electron number density (n_e) in AGN outflows: CII (e.g. Edmonds et al. 2011), NIII (e.g. Chamberlain & Arav 2015b), OIV (e.g. Arav et al. 2013), and NeVI and SiII (e.g. Borguet et al. 2012b). The method described below for SIV can be applied to the above ions as well.

The SIV* energy level is predominantly populated via

collisions of free electrons with SIV in the ground state (e.g., Leighly et al. 2009). Thus, the ratio of the column densities of SIV and SIV*, $N(\text{SIV})/N(\text{SIV}^*)$, can be used as an n_e diagnostic (e.g. Osterbrock & Ferland 2006, equations (3.20) and (3.23)):

$$n_e \simeq n_{\text{cr}} \left[\frac{2N(\text{SIV})}{N(\text{SIV}^*)} e^{-\Delta E/kT} - 1 \right]^{-1}, \quad (1)$$

where n_{cr} is the critical density for the excited and resonance energy levels of SIV, ΔE is the energy difference between the ground- and excited-state levels, k is the Boltzmann constant, and T is the temperature in Kelvin. The factor 2 comes from the ratio of degeneracies for the SIV* and SIV energy level, respectively. For plasma photoionized by a quasar spectrum, the region where SIV exists has $T \simeq 10^4 \text{ K}$ (see § 7.4), for which $e^{-\Delta E/kT} = 0.9$. For simplicity, for the discussion in this section, we assume $e^{-\Delta E/kT} = 1$, and in section § 7.4 we elaborate on the minor effect that a finite temperature will have on our results.

In practice, we deduce the n_e of the outflow by comparing the $N(\text{SIV}^*)/N(\text{SIV})$ ratio to predictions (see Fig. 1) made with ionic collision models that use the Chianti 8.0.2 atomic database (Dere et al. 1997; Del Zanna et al. 2015). Such a prediction is shown in the right panel of figure 1.

A photoionized plasma is characterized by the ionization parameter

$$U_{\text{H}} \equiv \frac{Q_{\text{H}}}{4\pi R^2 n_{\text{H}} c}, \quad (2)$$

where Q_{H} is the rate of hydrogen-ionizing photons emitted by the object, c is the speed of light, R is the distance from the central source to the absorber, and n_{H} is the total hydrogen number density. Using photoionization models, we can solve for U_{H} of a given quasar outflow (e.g. Arav et al. 2001; Hamann et al. 2001; Edmonds et al. 2011; Chamberlain et al. 2015a). Furthermore, in the outflow zone where SIV is abundant, the plasma is highly ionized, and $n_e \simeq 1.2 n_{\text{H}}$. Therefore, we can use equation (2) to solve for R . This is the procedure used for deriving R in most published results to date.

2.1. The Ideal Apparent Optical Depth Case

As described above, the ratio of occupied excited states to occupied ground states is a sensitive diagnostic for n_e (see Fig. 1) and thus R . For the apparent optical depth (AOD) case (where the residual intensity $I = e^{-\tau}$), $N(\text{SIV})$ and $N(\text{SIV}^*)$ can be straightforwardly extracted from the troughs (e.g., see equation (1) in Arav et al. 2003). Their ratio is then plotted on the theoretical curve (see Fig. 1), and n_e can be readily determined. There are two complications to address. First, there is contamination from Ly α forest absorption features, which is best addressed by using smooth templates to fit the SIV and SIV* troughs (see Borguet et al. 2012b, 2013; Chamberlain et al. 2015a). The smooth SIV and SIV* optical depth templates used in the references above had the same functional form (as a function of velocity) up to a scalar scale factor (SF). The templates gave good fits for the troughs in these high-quality X-shooter data,

and therefore motivated us to use a similar approach in this study as well.

The second complication is that at high n_e values, the ratio $N(\text{SIV}^*)/N(\text{SIV})$ approaches an asymptotic value (the Boltzmann ratio), and thus small errors in $N(\text{SIV}^*)$ and $N(\text{SIV})$ will create large uncertainties in the n_e estimate. In the right panel of figure 1, we conceptually demonstrate this issue. The error bars on n_e are derived by the crossing point of the \pm errors with the theoretical ratio curve. Therefore, the high-ratio case has a strong asymmetric uncertainties in n_e .

2.2. The Realistic Nonblack Saturation Case

Extracting reliable $N(\text{SIV})$ and $N(\text{SIV}^*)$ from an outflow's spectrum is complicated by the phenomenon of nonblack saturation. Using ionic doublet and multiplet troughs, it has been shown extensively that AOD-extracted N_{ion} often underestimates the actual N_{ion} , even in cases where the absorption features are fully resolved spectroscopically (e.g. Arav 1997; Arav et al. 1999, 2003, 2008), sometimes by as much as a factor of 1000 (Borguet et al. 2012b). With the possibility of nonblack saturation, we need to carefully assess the information available about $N(\text{SIV})$ and $N(\text{SIV}^*)$ that is embedded in their troughs.

For resonance doublets (e.g., C IV $\lambda\lambda 1548, 1551$), which arise from the same energy level, the real optical depths of the troughs obey the ratio $\tau(\text{CIV}1548\text{\AA})=2\tau(\text{CIV}1551\text{\AA})$ due to the ratio of their oscillator strengths. For SIV, the 1062 and 1073\AA transitions arise from separate energy levels with different electron populations. Therefore, there is no a priori relationship between their real optical depths. However, as we show below, even after accounting for the possibility of nonblack saturation, we can extract definitive constraints about n_e from the observed depth ratio of the SIV and SIV* troughs.

We define $N(\text{SIV}^*)_{\text{AOD}}$ and $N(\text{SIV})_{\text{AOD}}$ as the column densities derived for each trough using the AOD method; we also define the value of n_e determined from the ratio of these two column densities as n_{AOD} (see right panel of Fig. 1). For a case where the SIV trough is deeper than the SIV* one, $N(\text{SIV})_{\text{AOD}} > N(\text{SIV}^*)_{\text{AOD}}$, and vice versa. Once we detect an SIV $\lambda 1062$ trough, there are three cases that cover all physical possibilities, detailed as follows.

2.2.1. The SIV* $\lambda 1073$ trough Is shallower than the SIV $\lambda 1062$ trough

To investigate the effects of saturation, we use the standard partial-covering model (e.g., see § 3.2, in Edmonds et al. 2011), which assumes that an absorber with a single-value optical depth partially covers a single homogeneous emission source. For this case, the normalized residual intensity observed for the SIV and SIV* troughs (I_0 and I_* , respectively) as a function of the radial velocity v can be expressed as (see equation (1) in Edmonds et al. 2011)

$$I_0(v) = 1 - C(v) + C(v)e^{-\tau_0(v)} \quad (3)$$

$$I_*(v) = 1 - C(v) + C(v)e^{-\tau_*(v)} \quad (4)$$

where $C(v)$ is the fraction of the emission source covered by the absorber (we assume that $C(v)$ is the same

for SIV and SIV* as they arise from the same ion). When the SIV trough is deeper than the SIV* one, $I_0(v) < I_*(v)$, and the physical range of the covering factor is $1 - I_0(v) < C(v) < 1$. For $C(v) = 1$ we retrieve the AOD case ($\tau_0(v) = -\ln[I_0(v)]$ and ($\tau_*(v) = -\ln[I_*(v)]$). The case of maximum saturation is when $C(v) = 1 - I_0(v)$ for which equation (3) yields $\tau_0(v) \rightarrow \infty$. In contrast, for the same case, equation (4) yields a finite $\tau_*(v) = -\ln[I_*(v) - I_0(v)]$. For the example given by the solid and dashed blue lines in figure 1, at the bottom of the troughs, $\tau_0(v)_{\text{AOD}} = 1$, while $\tau_*(v)_{\text{AOD}} = 0.5$. For the same troughs, the case of maximum saturation yields $\tau_*(v) = 0.97$, while $\tau_0(v) \rightarrow \infty$.

This example illustrates the general case that can be deduced straightforwardly from equations (3) and (4):

$$\frac{\tau_*(v)}{\tau_0(v)} \leq \frac{\tau_*(v)_{\text{AOD}}}{\tau_0(v)_{\text{AOD}}} < 1. \quad (5)$$

The column density derived for each trough is proportional to the integrated optical depth over the width of the trough and inversely proportional to $f\lambda$, where f and λ are the oscillator strength and wavelength of the transition that gives rise to the trough. For the SIV and SIV* troughs we analyze, the f values are the same, and the difference in λ is less than 1%. Combing this assertion with equation (5), for the case where $I_0(v) < I_*(v)$ we obtain

$$\frac{N(\text{SIV}^*)}{N(\text{SIV})} \leq \frac{N(\text{SIV}^*)_{\text{AOD}}}{N(\text{SIV})_{\text{AOD}}} < 1, \quad (6)$$

and therefore equation (1) yields $n_e \leq n_{\text{AOD}} < n_{\text{cr}}$.

As discussed above, when the SIV* trough is shallower than the SIV trough, only the SIV trough can be highly saturated, and therefore the ratio $N(\text{SIV}^*)/N(\text{SIV})$ can approach 0. So, in principle, n_e can be very small (see right panel in Fig. 1). However, the photoionization solution for the outflow using other measured ionic column densities (e.g., see Figures 6 and 7, and accompanying discussion in Borguet et al. 2012b) will put an upper limit on $N(\text{SIV})$, which can then be used to derive $N(\text{SIV}^*)$ and obtain a lower limit for the $N(\text{SIV}^*)/N(\text{SIV})$ ratio. We define the n_e associated with this limit as n_{PI} : the lower limit on n_e that arises from photoionization modeling. The upper limit for the $N(\text{SIV}^*)/N(\text{SIV})$ ratio is given by $N(\text{SIV}^*)_{\text{AOD}}/N(\text{SIV})_{\text{AOD}}$, and therefore the upper limit for n_e is n_{AOD} . Thus, we obtain a range of possible n_e values $n_{\text{PI}} < n_e < n_{\text{AOD}}$ (shown as the shaded blue region in Figure 2).

An extreme version of this case is where an SIV* $\lambda 1073$ trough is not detected, and therefore only an upper limit $N(\text{SIV}^*)_{\text{UL}}$ can be obtained. For that case,

$$\frac{N(\text{SIV}^*)}{N(\text{SIV})} \leq \frac{N(\text{SIV}^*)_{\text{UL}}}{N(\text{SIV})_{\text{AOD}}}, \quad (7)$$

and only an upper limit on n_e can be obtained.

It is straightforward to show that equations (5)-(7) also apply to inhomogeneous absorption models of outflows' troughs (e.g. de Kool et al. 2002b; Arav et al. 2005, 2008).

2.2.2. The SIV* $\lambda 1073$ Trough Is Deeper than the SIV $\lambda 1062$ Trough

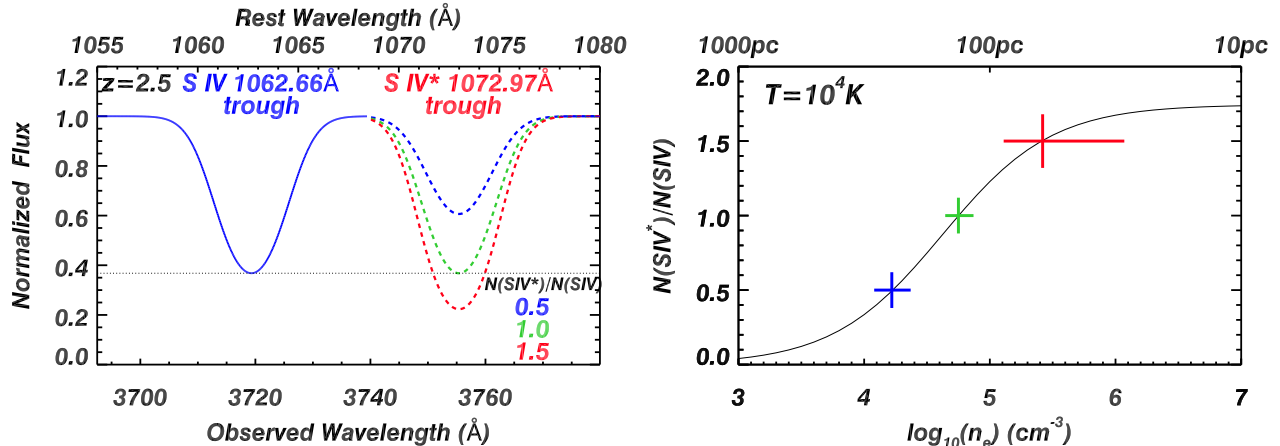


Figure 1. **Left:** For a given S IV trough (blue solid line), there are three qualitatively different possibilities for the S IV* trough (dashed lines), which are discussed in § 2.2 (the 0.5 and 1.5 values are only for illustrative purposes). **Right:** For the AOD case, the column densities of the S IV and S IV* troughs can be directly measured, and their ratio yields n_e (see Equation 1). This n_e value, combined with a determination of U_H (see Equation 2), yields the distance of the outflow from the central source. For a typical S IV outflow in a luminous quasar, the resultant distance is displayed on the top x-axis (see § 2.3).

An example of this case is shown by the red dashed line in the left panel of Fig. 1. For this case,

$$\frac{N(\text{S IV}^*)}{N(\text{S IV})} \geq \frac{N(\text{S IV}^*)_{\text{AOD}}}{N(\text{S IV})_{\text{AOD}}}. \quad (8)$$

This is again because the deeper trough is always more saturated than the shallower trough. However, there is an important physical difference in this case. The maximum value of $N(\text{S IV}^*)/N(\text{S IV})=2$, which is the ratio of degeneracies of the two energy levels. Moderate saturation can easily yield $N(\text{S IV}^*)/N(\text{S IV})=2$ for any case where the S IV* $\lambda 1073$ trough is deeper than the S IV $\lambda 1062$ trough. Therefore, in this case, $n_{\text{cr}} < n_{\text{AOD}} < n_e$ (see red arrow in Fig. 2).

2.2.3. The S IV* $\lambda 1073$ Trough Is Equal in Depth to the S IV $\lambda 1062$ Trough

This occurrence is shown by the green dashed line in Fig. 1). For this case, $N(\text{S IV}^*)/N(\text{S IV})$ can be both larger and smaller than $N(\text{S IV}^*)_{\text{AOD}}/N(\text{S IV})_{\text{AOD}}$. This will depend on which trough is more saturated, which cannot be determined in this case. Thus, n_e could have any value above n_{cr} . The lower limit for n_e is n_{PI} , as described in § 2.2.1. The allowed region is shown as the green shaded region in figure 2, and higher values of n_e to the right of the plot boundary are also allowed.

2.3. Distance Constraints from the S IV and S IV* Troughs Analysis

In § 2.2, we obtained constraints on n_e while taking into account the possibility of nonblack saturation in the S IV and S IV* troughs. We can convert these n_e constraints to constraints on R as follows. For a given outflow, knowledge of U_H and n_e determines R (see equation 2 and accompanying discussion). However, with the limited signal-to-noise (S/N) ratio and spectral resolution of the SDSS data, it is difficult to derive reliable determinations of ionic column density from outflow troughs and therefore obtain U_H solutions for individual outflows. Also, the best we can do for constraining n_e is to classify the outflows into one of the three categories discussed

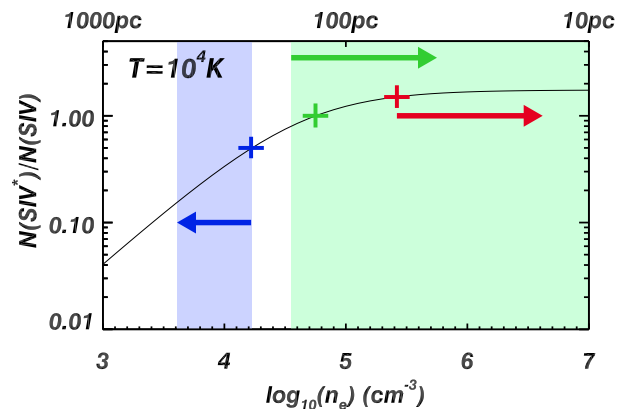


Figure 2. Realistic nonblack saturation case (see § 2.2). The ratio of S IV* to S IV column densities, $N(\text{S IV}^*)_{\text{AOD}}/N(\text{S IV})_{\text{AOD}}$, derived using the AOD method can be used to put important constraints on R (see § 2.3). When $N(\text{S IV}^*)_{\text{AOD}}/N(\text{S IV})_{\text{AOD}} < 1$ (blue cross), the blue shaded region shows the allowed R range. The AOD ratio sets the lower limit on R . If an S IV* trough is detected, an upper limit can be obtained from photoionization modeling. If a S IV* trough is not detected, only a lower limit on R can be obtained using the upper limit for $N(\text{S IV}^*)_{\text{AOD}}$. If $N(\text{S IV}^*)_{\text{AOD}}/N(\text{S IV})_{\text{AOD}} = 1$ (green cross), we can only set an upper limit on R (leftmost part of the green shaded region), again using photoionization modeling. When $N(\text{S IV}^*)_{\text{AOD}}/N(\text{S IV})_{\text{AOD}} > 1$ the red cross yields the upper limit on R .

in § 2.2: outflows that have $n_e < n_{\text{cr}}$ (§ 2.2.1), outflows where $n_e > n_{\text{cr}}$ (§ 2.2.2), and outflows where n_e can be larger than n_{cr} (§ 2.2.3),

With these three cases in mind, and lacking individual R determinations, we need to find a representative R for $n_e=n_{\text{cr}}$ and assess the plausible scatter around this value for individual objects. For high-luminosity quasars, there are four S IV outflows in the literature where detailed photoionization solutions are available (three can be found in table 5 of Borguet et al. 2013 and the fourth in table 5 of Chamberlain et al. 2015a). The value of R for each outflow was calculated using the n_e found for it. Therefore, using equation (2), it is straightforward to

Table 1
Distance from the central source based on an observed S IV 1062Å Trough.

S IV* 1073Å Trough	n_e	Constraint on R (pc)
Undetected	$n_e < n_{\text{AOD}} < n_{\text{cr}}$	$1000 < R$
Shallower than S IV	$n_{\text{PI}} < n_e < n_{\text{AOD}} < n_{\text{cr}}$	$100 < R < R_{n_{\text{PI}}}$
Similar depth to S IV	$n_{\text{PI}} < n_e$	$R < R_{n_{\text{PI}}}$
Deeper than S IV	$n_{\text{cr}} < n_{\text{AOD}} < n_e$	$R < 100$

Note. — For the definitions of n_{AOD} and n_{cr} see § 2.2; for n_{PI} see the first paragraph of § 2; and for $R_{n_{\text{PI}}}$ see § 2.3.

derive R for $n_e=n_{\text{cr}}$ for each outflow. We find an average value of $R(n_e=n_{\text{cr}})=200$ pc for these four outflows, where the individual values of $R(n_e=n_{\text{cr}})$ span the range 100–400 pc. Recent results from the full analysis of our VLT/X-shooter sample (Xu et al., 2018, ApJ submitted) agree with the above $R(n_e=n_{\text{cr}})$ values (see elaboration in §3.2).

We note that shielding-gas photoionization models (Murray et al. 1995) yield much higher U values for quasar outflows (and therefore smaller R for a given n_e). However, the shielding models cannot reproduce the full set of extracted ionic column densities from high-quality observations of outflows (e.g., Hamann et al. 2013). Therefore, we make use of models that are able to adequately model observed outflows by reproducing the measured value of their trough’s ionic column densities (i.e., Borguet et al. 2013; Chamberlain et al. 2015a, for actual S IV outflows).

The four objects mentioned above span magnitude and redshift ranges of $18.36 \geq r_{\text{mag}} \geq 17.65$ and $3.038 \geq z \geq 2.076$, respectively. These ranges are similar to the ranges found for our SDSS and X-shooter samples, $18.46 \geq r_{\text{mag}} \geq 17.47$ and $3.180 \geq z \geq 2.004$. Hence, the scatter of $R(n_e = n_{\text{cr}})$ in our samples should be similar. Therefore, we expect that for the large majority of the S IV outflows in our samples, $R(n_e=n_{\text{cr}})>100$ pc, and we use $R(n_e=n_{\text{cr}})=100$ pc as a lower limit. In § 5.3 we show that for cases where a S IV* trough is not detected [$N(\text{S IV}^*)_{\text{AOD}}/N(\text{S IV})_{\text{AOD}} \lesssim 0.1$], $R \gtrsim 1000$ pc.

In table 1 we summarize the n_e and R constraints that can be deduced for a high-luminosity quasar where an S IV 1062Å outflow trough is observed. We use the full constraints detailed in § 2.2 and define $R_{n_{\text{PI}}}$ as the distance of the outflow when $n_e=n_{\text{PI}}$.

3. S IV SURVEY SAMPLES

Using the SDSS data release 7, the final release of SDSS-II (Schneider et al. 2010), Dunn et al. (2012) compiled a sample of 156 bright quasars covering the S IV and S IV* spectral region. They found three quasar outflows that show both S IV and S IV* troughs (a fraction of 1.9%). However, the Dunn et al. (2012) survey does not yield information about the distribution of R in quasar outflows. The number of S IV outflows (three) is too small for a census, and more importantly, the criterion therein requiring the existence of both S IV and S IV* causes a bias against weak or nonexistent S IV* troughs, leading to uncertainty in the census of R values. In this paper, we overcome these shortcomings by conducting an SDSS S IV survey using a sample eight times larger than that of Dunn et al. (2012), and requiring only an identification of the S IV trough.

We also analyze a sample of objects observed with the VLT/X-shooter spectrograph, which has the advantage of much better data than the SDSS spectra.

3.1. The SDSS Sample

The final released quasar catalog of SDSS-III has been made publicly available through the SDSS website². This catalog is a product of the intensive visual inspection of SDSS optical spectra from the twelfth data release (DR12; Alam et al. 2015) undertaken by Pâris et al. (2017). Using this catalog, we construct our sample by selecting all the quasars satisfying the following criteria.

1. The r -band magnitude, obtained through point spread function (PSF) fitting, is required to be brighter than 18.5, which facilitates an S/N ratio high enough for performing absorption-line identification and kinematic analysis.
2. the spectral coverage of the SDSS and BOSS spectrographs are 3800–9100Å and 3600–11000Å, respectively. The redshift (visually adjusted by Pâris et al. 2017) is required to be higher than 2.8 for SDSS quasars and 2.6 for BOSS quasars. At such redshifts, we obtain spectral coverage down to 1000Å in the rest frame for a BOSS $z = 2.6$ and for an SDSS $z = 2.8$ quasars, so the region of an S IV 1063Å outflow up to at least 17,000 km s⁻¹ can be probed.

Among the resultant 1091 quasars, we search for relatively broad (FWHM $\gtrsim 500$ km s⁻¹) and deep troughs (minimum residual intensity less than 0.5) between the wavelength of the observed C IV and Si IV broad emission lines. This strategy avoids the narrower intervening systems and will find all C IV BALs and mini-BALs (see definitions in § 4.1) with velocities between 0 and –30,000 km s⁻¹. We find such absorption systems in 191 objects. This fraction, 18%, is close to the 16% found by Dunn et al. (2012) for similar-width troughs. We focus our detailed visual inspection on these 191 quasars, because the emergence of S IV absorption without a significant C IV trough is not expected (see Dunn et al. 2012), and the C IV region, by definition, has been the benchmark for characterizing absorption troughs in AGN outflows for decades (e.g. Weymann et al. 1981, 1991).

3.2. The VLT/X-shooter Sample

² <http://data.sdss3.org/datamodel/files/BOSS-QSO/DR12Q/DR12Q.html>

Our SDSS/BOSS survey has the advantage of a large number of objects. However, the modest spectral resolution and S/N ratio of the SDSS/BOSS quasar data make the identification of the S IV and S IV* troughs challenging, especially for the narrower troughs. We therefore conducted a complementary survey using the X-shooter spectrograph on the VLT. To avoid selection biases that might give preference to a specific ratio of S IV*/S IV trough depths (and therefore R), we conducted a blind survey. We chose 13 SDSS objects at redshifts lower than 2.5 so that the SDSS data did not show the spectral region of the S IV and possibly S IV* troughs. Our two other selection criteria were (a) bright objects, to obtain a high S/N in a reasonable exposure time, and (b) deep Si IV outflow troughs, to increase the likelihood of detecting S IV and S IV* troughs.

Without prior knowledge of their spectral region, the S IV and S IV* troughs' depth ratio can fall into any of the categories described in sections 2.2.1, 2.2.2 and 2.2.3. For example, if a large majority of the outflows are situated at $R < 1$ pc, photoionization models will require $n_e \gg n_{cr}$, and every S IV trough will be accompanied by an equal or deeper S IV* trough (see § 2.2, and Fig. 2). Seven out of the 13 objects in the X-shooter sample showed S IV outflow troughs (a total of eight outflows).

Recent results from the full analysis of this VLT/X-shooter sample (Xu et al., 2018, ApJ submitted) show that the average value of $R(n_e=n_{cr})=250$ pc for these eight outflows, where the individual $R(n_e=n_{cr})$ values span the range 80–600 pc. This is in full agreement with the findings described in § 2.3.

4. IDENTIFICATION OF S IV ABSORPTION TROUGHS

To identify absorption troughs associated with a quasar outflow, we begin with the C IV doublet $\lambda\lambda 1548.20, 1551.77$. After identifying C IV trough(s) with velocities between 0 and $-30,000$ km s⁻¹ in the rest frame of the quasar, we look for kinematically corresponding absorption features from the Si IV $\lambda\lambda 1394.76, 1403.77$ doublet. We use the kinematic structure of the Si IV troughs as our guide for the existence of an S IV absorption trough. We do so for two reasons. First, experience shows that an S IV absorption trough is never detected if an Si IV trough is not detected; second, the Si IV trough profile shows good kinematic correspondence with the S IV trough profile (Dunn et al. 2012; Borguet et al. 2012b, 2013; Chamberlain et al. 2015a).

The existence of Ly α forest absorption troughs is the primary obstacle when trying to identify S IV absorption troughs in the spectra of the $z > 2.6$ quasars. The intrinsic line widths of Ly α absorbers are broadened by the ~ 160 – 180 km s⁻¹ spectral resolution of the SDSS and BOSS spectrographs (at the typical observed wavelength of S IV lines), as well as by random clumping of Ly α forest troughs. To minimize the confusion due to the Ly α forest, we require that the Si IV troughs have a velocity width of at least 500 km s⁻¹ for the SDSS and BOSS data (we lessen this requirement for the higher-resolution VLT/X-shooter data).

4.1. Visual template fitting

Often, the Si IV outflow troughs show a complex kinematic morphology. We identify a Si IV outflow component as a kinematic structure that has a local minimum

of $I < 0.7$, and whose width is larger than 500 km s⁻¹. Several of our surveyed quasars produce two and even three such Si IV outflow components. In most cases, we create an AOD template for each individual component based on the Si IV 1402.77Å trough. In the AOD case, the residual intensity is $I = e^{-\tau}$; therefore, our template is given by

$$\tau(\lambda)_{1402.77} = -\ln[I(\lambda)_{1402.77}], \quad (9)$$

where the subscript 1402.77 denotes that the absorption feature is identified as arising from the Si IV 1402.77Å line. In cases where the Si IV 1402.77Å absorption is strongly blended with the absorption of a different velocity component arising from the Si IV 1393.76Å line, we use the Si IV 1393.76Å trough at the original velocity as a template.

We then make the assumption that the S IV trough will have the same kinematic profile as $\tau(\lambda)_{1402.77}$, scaled by a constant factor. This assumption works fairly well for cases where the saturation in the Si IV trough is less than a factor of two [i.e., $\tau(\text{real}) < 2\tau(\text{AOD})$]. In § 7 we elaborate on more saturated cases.

To identify an S IV 1062.66Å trough associated with the outflow component identified by the Si IV absorption, we simply transform the template to the expected wavelength of the S IV trough.

$$\lambda_{\text{S IV expected trough}} = \lambda_{\text{Si IV trough}} \frac{1062.66}{1402.77}. \quad (10)$$

A continuum-plus-emission-line model is a prerequisite for template-fitting as we need to work with residual intensities. We construct this model by visually depicting the overall continuum with a power law and adding a Gaussian profile where an emission-line feature (the most relevant ones are associated with the Si IV $\lambda\lambda 1394, 1403$ and O VI $\lambda\lambda 1032, 1038$ doublets) is present. Although O VI emission is assumed to be present in every case, if the spectrum is free of absorption lines, we adopt a conservative strategy that when O VI emission is completely unseen in the data, we do not artificially create it in this model. This avoids a significant arbitrariness and uncertainty in the derived emission model.

When an emission model consisting of a power law and a number of Gaussians (at different wavelengths) fails to present a reasonable fit, we do a manual cubic spline fit instead. We then produce the residual intensity spectrum by dividing the fluxed spectrum by the emission model.

As described above, to account for the difference in optical depth between the Si IV and S IV troughs, we apply an SF to the $\tau(\lambda)_{1402.77}$, to best fit the S IV absorption feature according to our visual inspection.

Due to the frequent contamination from Ly α forest absorbers, sometimes only a portion of the velocity profile of the Si IV template can be matched to the S IV trough. When this situation occurs, we limit our template to being situated predominantly on and above the actual data, because any portion of the template located below the actual data is nonphysical (with the uncertainty of spectroscopic measurement taken into account). We then repeat the process for identifying a possible S IV* 1072.96Å trough while allowing for a different SF than that used for the S IV trough. The error on the SF values is calculated

Table 2
Our SDSS quasar sample with detected Si IV λ 1063
absorption trough(s).

RA, Dec (1)	Plate-MJD-fiber (2)	z (3)	r (4)
07:57:15.34 +21:33:33.8	4482-55617-760	2.965	18.17
09:13:07.82 +44:20:14.4	4687-56369-700	2.930	18.02
09:37:10.77 +25:57:20.0	5791-56255-652	2.711	18.41
09:58:58.14 +36:23:19.0	4637-55616-580	2.671	17.78
11:31:32.86 +49:28:14.0	6685-56412-853	2.625	18.14
11:45:25.74 +23:59:40.4	6422-56328-909	2.714	18.09
* 11:45:48.38 +39:37:46.7	4654-55659-856	3.108	17.94
12:14:20.10 +51:49:25.1	6682-56390-108	2.630	18.42
^m 12:20:17.06 +45:49:41.2	6640-56385-266	3.275	18.18
12:26:54.39 -00:54:30.6	3792-55212-716	2.611	18.37
12:37:54.83 +08:41:06.8	5406-55955-204	2.859	17.47
^m 13:38:04.79 +47:32:19.9	6748-56371-880	2.630	17.66
* 13:47:22.83 +46:54:28.5	6749-56370-348	2.915	17.98
14:07:45.50 +40:37:02.3	5169-56045-616	3.180	18.48
14:22:40.79 +21:26:44.4	5898-56045-232	3.023	18.47
15:03:32.18 +36:41:18.1	5168-56035-253	3.257	17.87
* 15:09:23.38 +24:32:43.3	6019-56074-110	3.045	17.48
15:43:54.87 +49:27:21.4	6723-56428-436	2.625	17.67
15:50:47.65 +58:07:34.8	6785-56487-216	3.070	18.33
16:42:19.88 +44:51:24.0	6031-56091-588	2.893	17.86
17:03:22.42 +23:12:43.3	4177-55688-250	2.626	18.40
22:30:06.55 +21:59:08.5	6118-56189-832	2.870	18.30
23:35:31.98 +04:44:33.3	4283-55864-942	3.160	18.46
23:41:50.01 +14:49:06.1	6138-56598-406	3.165	18.43
23:51:53.80 -06:18:30.2	7146-56573-716	2.780	18.26

Note. — (1) Right ascension and declination (epoch 2000). (2) SDSS spectrum identifiers, including plug plate number, Julian Date, and fiber number. (3) The quasar redshifts adopted here are those visually adjusted by Pâris et al. (2017). (4) The r -band magnitude obtained through PSF fitting.

* Objects already found by Dunn et al. (2012).

^m Objects classified as mini-BALs (see text).

using the average flux error per resolution element over the spectral region of the template (defined as 1σ). We calculate the SF associated with shifting the template by $\pm 1\sigma$ and report the difference between these values and the fitted SF as the errors.

In Table 2, we give details on the 25 quasars from our SDSS sample with detected Si IV λ 1063 absorption trough(s). Except for two, all the C IV troughs in these objects adhere to the width definition of a Broad Absorption Line (BAL); having a full width at 90% residual intensity larger than 2000 km s^{-1} (see Weymann et al. 1991). The remaining two objects have C IV troughs with widths between 500 and 2000 km s^{-1} and therefore are classified as mini-BALs (see Hamann & Sabra 2004). The two mini-BAL outflows are designated by "^m" in front of their right ascension.

Table 3 gives similar parameters for quasars from our VLT/X-shooter sample with detected Si IV λ 1063 absorption trough(s). There are five BAL and two mini-BAL outflows in this sample (the latter are designated by "^m" in front of their right ascension).

The manual template fits of all SDSS Si IV absorption outflows are shown in Fig. 3, while the outflows in our VLT X-Shooter quasar sample are treated in the same way in Fig. 4. The SF values denote the SFs (and their errors) by which we multiplied the $\tau(\lambda)_{1402.77}$ template to fit the Si IV and Si IV* troughs.

Notes on two objects are as follows.

Table 3
Our VLT/X-Shooter quasar sample with detected Si IV λ 1063
absorption trough(s).

R.A., Decl. (1)	Plate-MJD-Fiber (2)	z (3)	r (4)
00:46:13.54 +01:04:25.8	4223-55451-666	2.149	18.04
^m 08:25:25.07 +07:40:14.3	4866-55895-522	2.204	17.89
08:31:26.16 +03:54:08.1	4764-55646-244	2.076	18.27
09:41:11.12 +13:31:31.2	5318-55983-604	2.021	18.15
^m 11:11:10.15 +14:37:57.1	5362-56017-170	2.138	18.03
11:35:12.70 +16:15:50.7	2503-53856-138	2.004	18.36
15:12:49.29 +11:19:29.4	1718-53850-564	2.109	17.65

Note. — (1) Right ascension and declination. (2) SDSS spectrum identifiers, including plug plate number, Julian Date, and fiber number. (3) The redshifts adopted here are those visually adjusted by Pâris et al. (2017). (4) The r -band magnitude obtained through PSF fitting.

^m Objects classified as mini-BALs (see text).

J0937+2557. This is a case of strong saturation in the Si IV troughs, for which we mention above that the template method is not applicable. Therefore, we used the fact that Al III troughs are seen in this outflow and are clearly not strongly saturated and constructed an Al III template (see inset figure for the object in Fig. 3), which fits the data very well.

J1503+3641. In the spectrum of this object, there is a clear damped Ly α system, so we normalized the spectrum accordingly (see Fig. 3)

4.2. Quantifying the Goodness of Fit Using Monte Carlo Simulations

Figures 3 and 4 show a compelling qualitative case for the identification of Si IV troughs. In all cases, the Si IV absorption template transformed to the expected wavelength of the Si IV trough shows a good match with an observed absorption feature. The template can be fitted to the observed absorption feature using a single free parameter multiplying the Si IV optical depth template as a whole. In most cases, this procedure shows a compelling Si IV trough at the expected position.

To quantify the goodness of the Si IV template fits, we carry out Monte Carlo Simulations of automated template fitting. We select a wavelength range in the vicinity of the Si IV/Si IV* lines (typically 1038–1105 Å rest frame, avoiding the prominent absorption troughs arising from the O VI $\lambda\lambda$ 1032, 1038 doublet) and transform the Si IV template onto a random wavelength position within this range. We then progressively increase the depth of the template until any part of it reaches the actual spectral data. We consider any portion of the template below the data as unphysical, though we allow a 3σ tolerance level, where σ is the uncertainty of the spectral flux density at each wavelength per pixel.

In particular, we perform the following iterative fitting procedure.

- We set the maximum optical depth (i.e. the deepest position) of the template to be 0.2 and determine if the template is below the actual data by 3σ or more within its wavelength range.
- If this situation occurs, the iteration is stopped, and we consider the trough to be too shallow to be physical and abandon this fit.

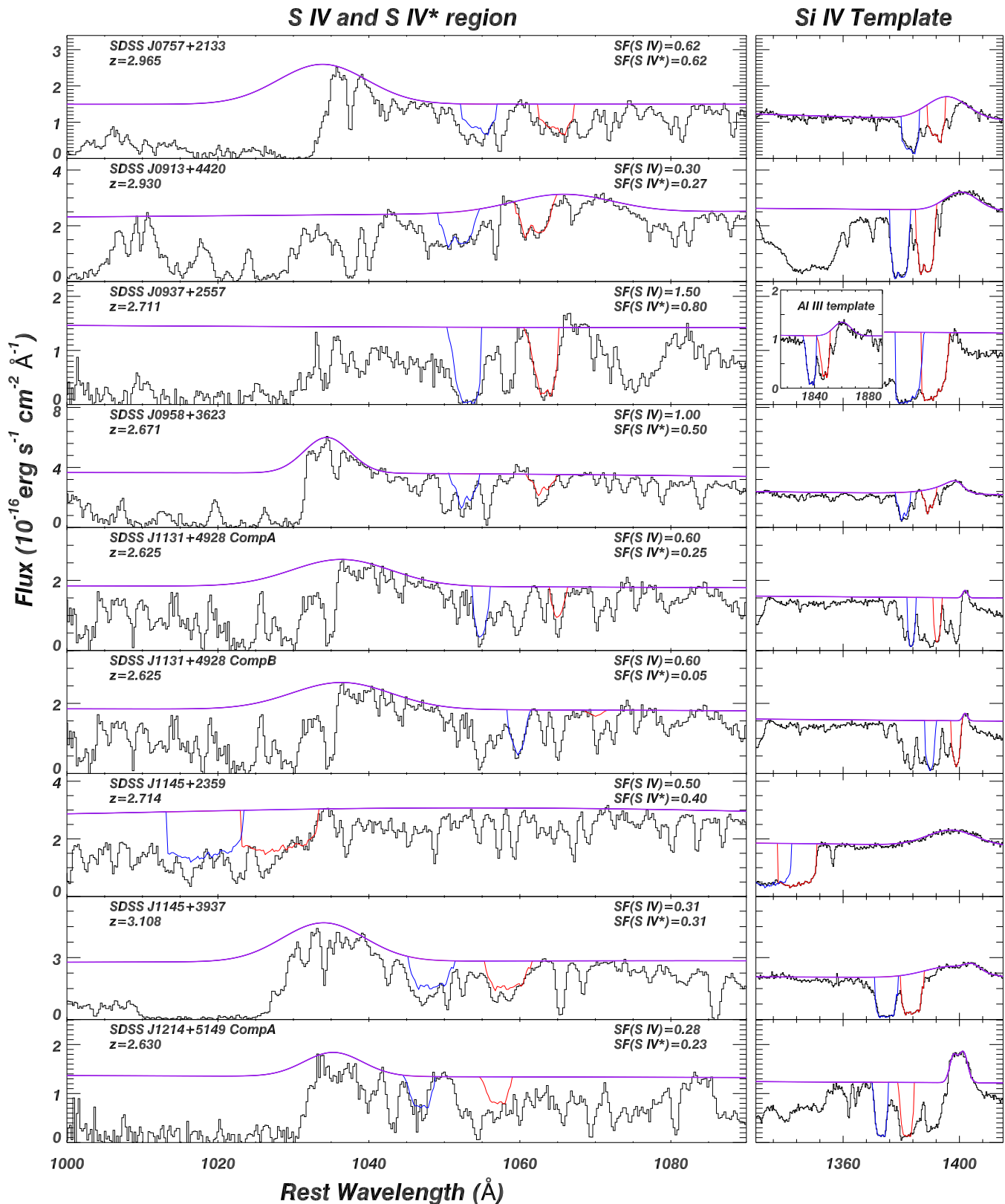


Figure 3. Visual template fitting. Each row shows a single outflow component, and the purple line shows the emission model. The right panel shows the Si IV outflow region, where the red line shows the absorption template for the Si IV 1402.77 Å line. In most cases, the blue line shows the fit of that template to the absorption feature of the same component caused by the stronger Si IV 1393.76 Å transition. The left panel shows the S IV and S IV* outflow region. In most cases, we transform the Si IV 1402.77 Å to the expected wavelength of the same component for the S IV and S IV* transitions. The blue trough shows the scaled Si IV 1402.77 Å template at the expected position for the S IV 1062.66 Å trough, and similarly, the red trough is for the expected position of the S IV* 1072.96 Å transition (see § 4.1). The SF that is applied to the AOD of the Si IV template is displayed for both the S IV and S IV* lines. In the text, we discuss the few cases where we use the absorption from the Si IV 1393.76 Å transition as a template, as well as the one case where we use the Al III template (see inset figure for quasar SDSS J0937+2557).

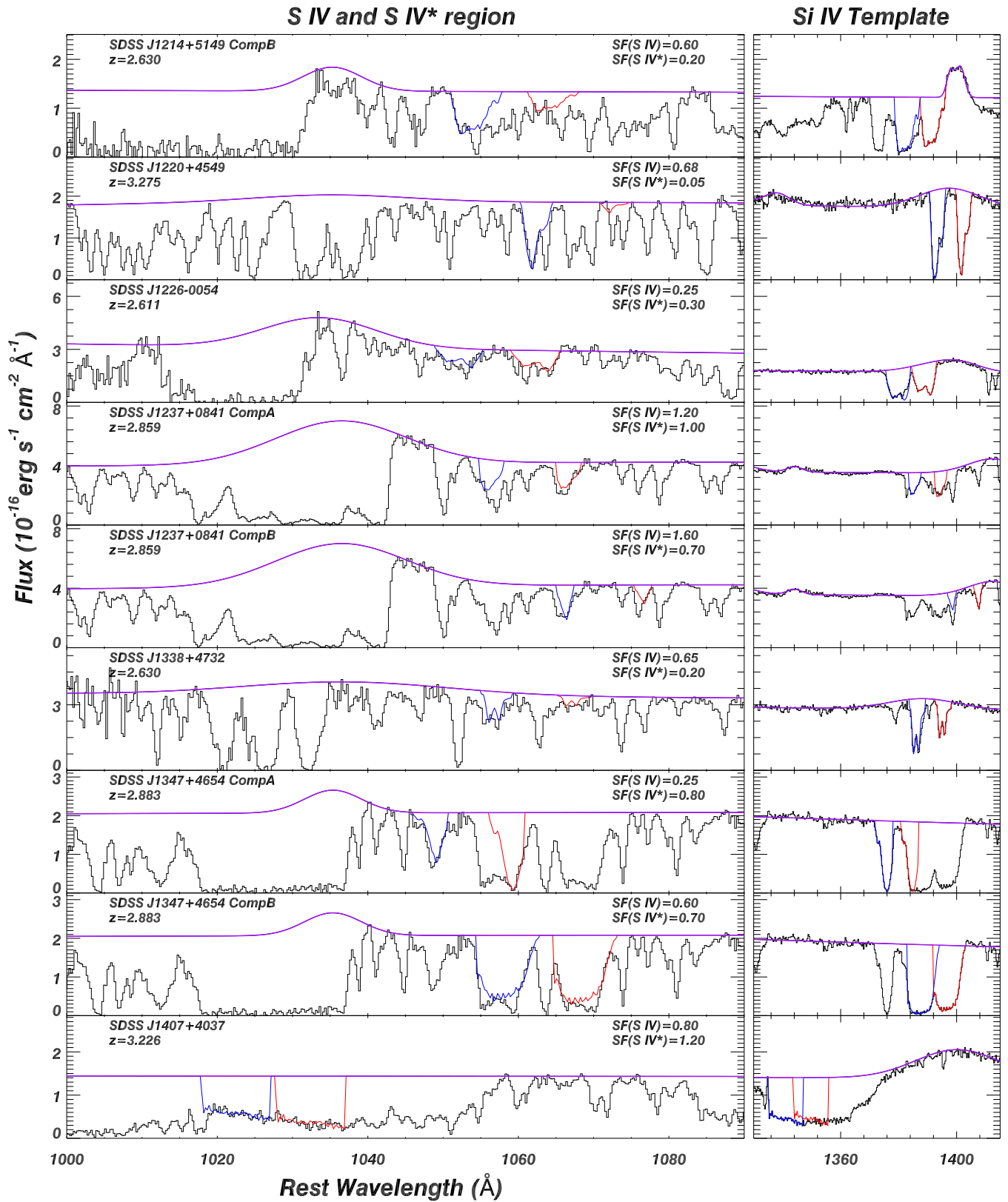


Figure 3. Continued.

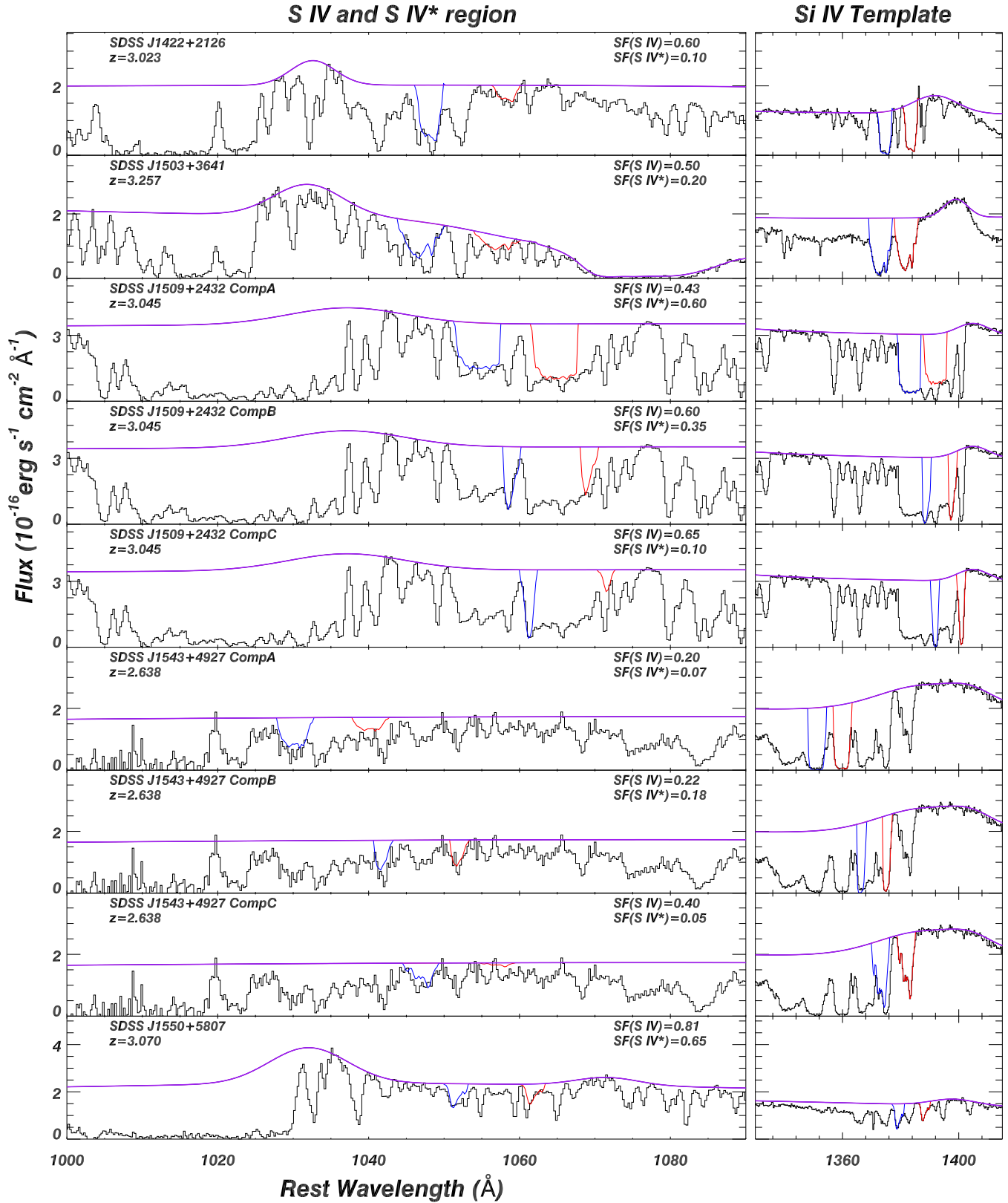


Figure 3. Continued.

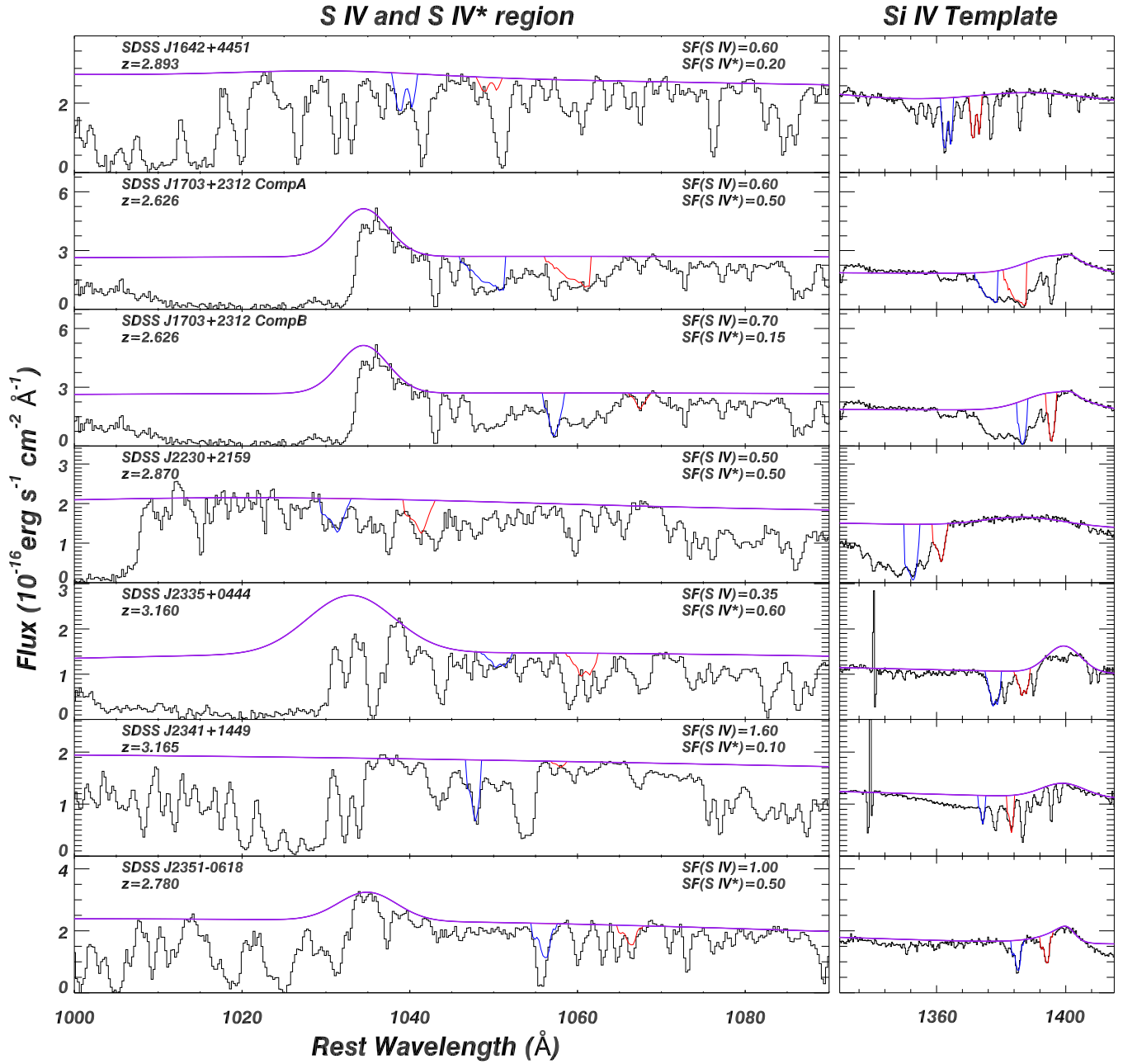


Figure 3. Continued.

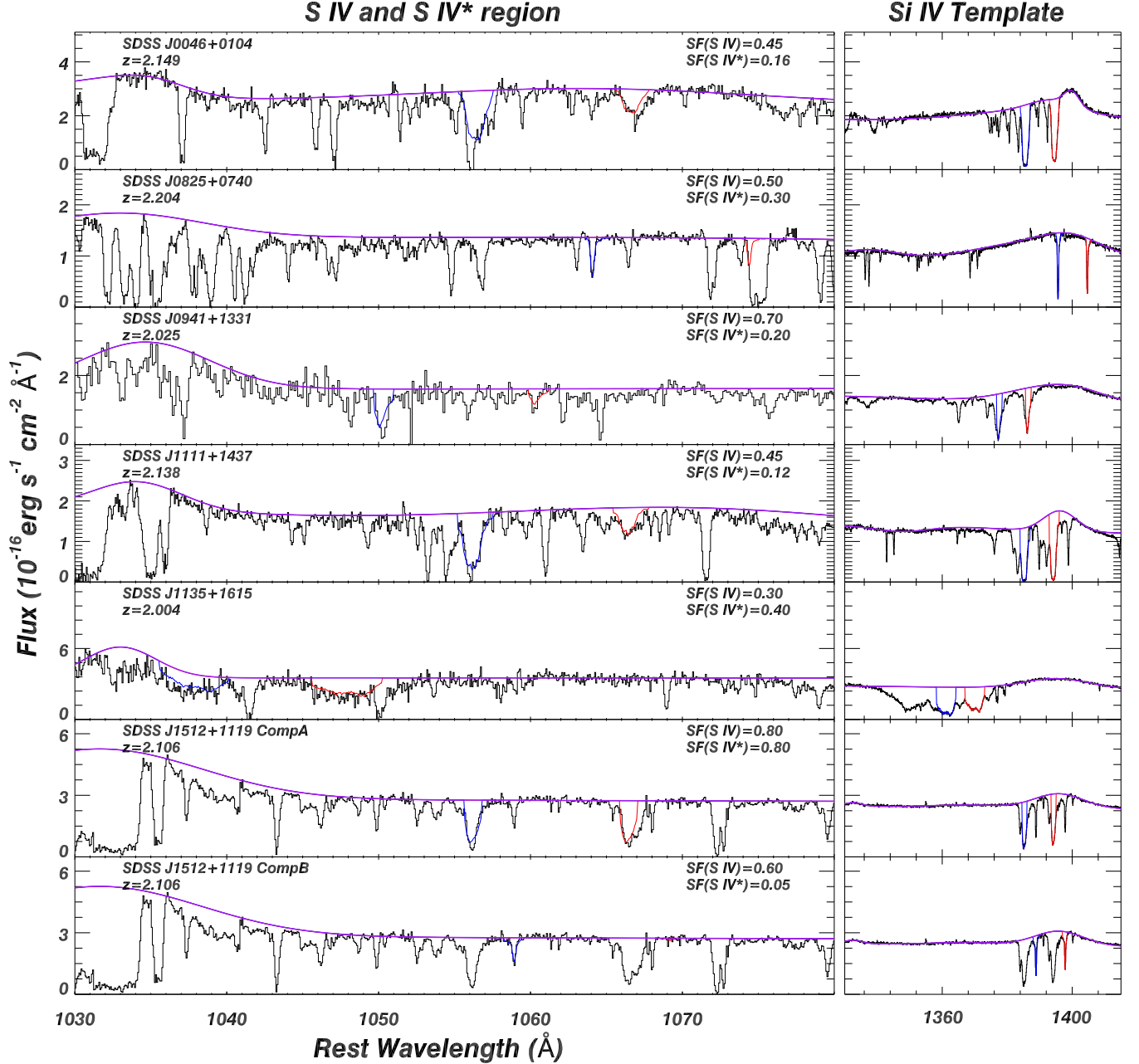


Figure 4. Similar presentation as in Fig. 3 but for our VLT X-Shooter quasar sample that shows S IV outflow troughs.

- If the whole template is above the spectral data (minus 3σ), we successively increase the maximum optical depth of the template by 0.01 each time. We iterate until the scaled template finally reaches the largest possible AOD before any portion dips 3σ below the data, which we take as the final fitting result. We then calculate a goodness-of-fit figure of merit, which is a modified reduced χ^2 (χ_{mod}^2 ; see below) for this final fit to the data.

We perform the above procedure at 1000 random wavelengths in the chosen 1038–1105 Å rest-frame range. We then use the same procedure for the template that is transformed to the exact position expected for an S IV 1062.66 Å trough (using equation (10)) and calculate the

χ_{mod}^2 of this “expected trough fit” as well. We do the same for the template that is transformed to the exact position expected for an S IV* 1072.96 Å trough.

4.2.1. Goodness-of-fit figure of merit

The identification of a of an S IV trough amidst the Ly α forest absorption rests on three considerations.

- 1) A significant absorption feature has to coincide with the exact spectral position predicted by the Si IV template (using equation (10)).
- 2) Not only does an absorption feature need to exist at that predicted wavelength position, but its shape has to match a significant portion of the scaled template.
- 3) Deeper absorption features adhering to points 1 and

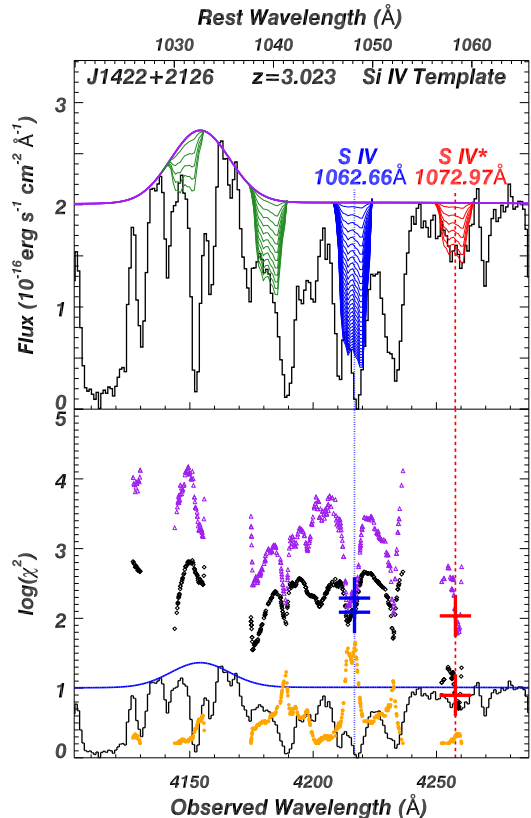


Figure 5. Example of our Monte Carlo simulations. Top panel: automated template fitting procedure shown for the expected positions of the S IV and S IV* troughs (blue and red, respectively) as well as for two random wavelength positions (green). Bottom panel: χ^2_{mod} for the Monte Carlo fits at each random wavelength (purple symbols). The χ^2_{mod} values for the expected S IV and S IV* troughs are shown by the blue and red crosses, respectively, and by green crosses for the two Monte Carlo simulations shown in the top panel. Yellow dots show the maximum optical depth of the fits at each wavelength.

2 are better candidates for an S IV trough amongst the myriad Ly α forest absorption features.

Using the standard $\chi^2 = (model - I)^2 / \sigma^2$ (where I is the residual intensity at the particular wavelength, model is the value of predicted I using the scaled template at the same wavelength, and σ is the error on the measurement) yields lower χ^2 values for shallow features when systematic effects dominate the fit. For example, if $I > 0.8$, then using our fitting procedure $(model - I)^2 < 0.04$ whereas for a deep feature with $I > 0.2$, $(model - I)^2 < 0.64$. Thus, inherently, shallow features will tend to have lower values of χ^2 .

We therefore introduce a modified χ^2 (χ^2_{mod}) that compensates for this deep trough effect by normalizing each point by the depth of the data.

$$\chi^2_{mod} \equiv \frac{1}{n-1} \sum_j \left[\frac{model(j) - I(j)}{\sigma(j)} \times \frac{1}{1 - I(j)} \right]^2, \quad (11)$$

where the sum J is taken over all the the points of the template and n is the number of degrees of freedom. It is important to note that the use of χ^2_{mod} as a goodness-of-fit measure does not give preference for S IV absorption features. Instead, it gives preference for deeper absorp-

tion features of all kinds, as is desirable when trying to identify distinct absorption features in data dominated by Ly α forest absorption features (see point 3 above)

The distribution of χ^2_{mod} from the 1000 random wavelengths is compared to the reduced χ^2_{mod} value of the expected trough fits. Cases where less than 10% of the random fits have smaller χ^2_{mod} than the expected trough fits are considered to be good fits for a S IV outflow trough.

Many times we find good fits for both S IV and S IV* outflow troughs. The chance probability of a random combined S IV and S IV* outflow trough fit is much lower than that for an individual trough fit. Many such cases can be seen in figures 3 and 4, which significantly strengthen the viability of the identification of these troughs amidst the Ly α forest.

In figure 5 we show an example of these simulations, and in Tables 4 and 5 we give this representative percentage for each outflow component, which gives a quantitative measure for the goodness of the template fit.

5. RESULTS

5.1. SDSS Sample

As we noted in § 3.1, from 1091 SDSS and BOSS quasars in our sample, 191 quasars show C IV outflow absorption troughs with velocity widths larger than 500 km s⁻¹. Of these 191 quasars, we found 25 that show robust detection of corresponding S IV outflow troughs, or 13%. This fraction is a lower limit, since (a) in many cases the data allow for the existence of an S IV trough, but a kinematic correspondence with the Si IV trough does not exist due to strong blending with Ly α forest absorption troughs; (b) due to the thick Ly α forest and limited S/N and spectral resolution, we do not identify S IV troughs with optical depths less than 0.3, therefore shallow S IV troughs are not identified. Several of the S IV quasars show two or three distinct outflow components, so in total, our survey yielded 34 S IV outflow components.

The analysis results for these components are shown in Table 4. In section 2 we demonstrated the following points.

1) For luminous quasars, outflows with $n_e < n_{cr}$ (where n_{cr} is the critical density for the excited and resonance energy levels of S IV) are situated at distances larger than 100 pc from the central source (see section 2.3).

2) When $N(S\ IV^*)_{AOD} / N(S\ IV)_{AOD} < 1$, that is when the S IV* trough is shallower than the S IV trough, $n_e < n_{cr}$ (see § 2.2). (Hereafter, we use $N(S\ IV^*) / N(S\ IV)$ to denote $N(S\ IV^*)_{AOD} / N(S\ IV)_{AOD}$, including in Tables 3 and 4.)

Since $N(S\ IV^*) / N(S\ IV)$ equals the ratio of the S IV to S IV* template SFs (see § 3), we can calculate the values for the former using the SF given in figure 3. In Table 4, we separate the values of $N(S\ IV^*) / N(S\ IV)$ into four physically motivated columns:

Column 5 gives $N(S\ IV^*) / N(S\ IV) > 1.2$, for which $n_e > n_{cr}$ and therefore $R < 100$ pc (corresponds to the last row in Table 1)

Column 6 gives $N(S\ IV^*) / N(S\ IV) \sim 1$, for which R can be smaller 100 pc. (the full constraints are discussed in §2.2.3 and summarized in the third row of Table 1). Taking into consideration the errors on $N(S\ IV^*) / N(S\ IV) \sim 1$, in this case, we grouped together in this case all of the

Table 4
Derived properties of S IV and S IV* Troughs in the SDSS quasar sample.

Object	v_{ctr}	Δv	$f(\chi^2)$	$1.2 < \frac{N(\text{S IV}^*)}{N(\text{S IV})}$	$0.8 < \frac{N(\text{S IV}^*)}{N(\text{S IV})} < 1.2$	$0.5 \leq \frac{N(\text{S IV}^*)}{N(\text{S IV})} < 0.8$	$\frac{N(\text{S IV}^*)}{N(\text{S IV})} < 0.5$
(1)	(2)	(3)	(4)	(5)	(6)	(7)	(8)
J0757+2133	-1950	1400	9.4%		1.00±0.15		
J0913+4420	-3440	1600	0.3%		0.90±0.09		
J0937+2557	-3160	2100	3.7%			0.53±0.08	
J0958+3623	-2950	1100	2.8%			0.50±0.09	
J1131+4928 A	-4070	700	0.4%				0.42±0.07
J1131+4928 B	-830	900	0.2%				0.08±0.07
J1145+2359	-13340	3000	(a)3.7%		0.80±0.12		
J1145+3937	-4570	1800	4.3%		1.00±0.12		
J1214+5149 A	-6900	1200	0.3%		0.82±0.28		
J1214+5149 B	-2900	1900	0.9%				0.33±0.12
J1220+4549	-220	1100	0.5%				0.07±0.04
J1226-0054	-2570	1800	3.0%		1.20±0.33		
J1237+0841 A	-3700	900	6.8%		0.83±0.08		
J1237+0841 B	-1060	600	8.4%				0.44±0.06
J1338+4732	-1860	1100	3.3%				0.31±0.17
J1347+4654 A	-5610	1300	0.2%	(b)3.20±0.45			
J1347+4654 B	-1670	2300	0.8%		1.17±0.11		
J1407+4037(c)	-11710	3400	8.6%	1.50±0.15			
J1422+2126	-3890	1100	3.8%				0.17±0.04
J1503+3641	-4550	1800	7.3%				0.40±0.10
J1509+2432 A	-2770	2400	3.2%	1.41±0.09			
J1509+2432 B	-1180	700	8.0%			0.58±0.04	
J1509+2432 C	-418	700	3.6%				0.15±0.03
J1543+4927 A	-9460	1400	2.9%				0.35±0.19
J1543+4927 B	-6010	700	3.4%		0.82±0.25		
J1543+4927 C	-4210	1300	8.3%				0.12±0.24
J1550+5807	-3230	800	5.2%		0.80±0.16		
J1642+4451	-6820	900	0.3%				0.33±0.15
J1703+2312 A	-5260	1500	2.2%		0.83±0.13		
J1703+2312 B	-1530	700	1.6%				0.21±0.04
J2230+2159	-8980	1100	5.7%		1.00±0.22		
J2335+0444	-3510	900	6.5%	1.71±0.50			
J2341+1449	-6220	500	3.9%				0.06±0.02
J2351-0618	-1850	700	4.2%			0.50±0.12	
Total population				4	12	4	14

Note. — (1) Abbreviated object name and outflow component. (2) Relativistic velocity (in km s⁻¹) of the S IV outflow in the quasar’s rest frame, measured at the deepest part of the absorption trough. (3) Full width at 90% of the S IV trough, measured from the line profile template constructed from the Si IV trough. (4) Fraction of Monte Carlo template fits giving a χ^2_{mod} smaller than the one obtained at the expected wavelength of the S IV 1062.66Å trough (obtained by using the same automated fitting procedure as our Monte Carlo simulation). (5)–(8) Value of $N(\text{S IV}^*)_{\text{AOD}}/N(\text{S IV})_{\text{AOD}}$, split among the four categories discussed in § 5.1. These values are calculated from the SFs of both troughs in our manual template fits shown in Figure 3. For (a), (b) and (c) - see § 5.1.1

Table 5
Derived properties of S IV and S IV* troughs in the VLT/XShooter quasar sample.

Object	v_{ctr}	Δv	$f(\chi^2)$	$1.2 < \frac{N(\text{S IV}^*)}{N(\text{S IV})}$	$0.8 < \frac{N(\text{S IV}^*)}{N(\text{S IV})} < 1.2$	$0.5 \leq \frac{N(\text{S IV}^*)}{N(\text{S IV})} < 0.8$	$\frac{N(\text{S IV}^*)}{N(\text{S IV})} < 0.5$
(1)	(2)	(3)	(4)	(5)	(6)	(7)	(8)
J0046+0104	-1746	606	1.4%				0.36±0.06
J0825+0740	+406	200	0.4%			0.60±0.18	
J0831+0354	-10800	1350	0.3%			0.72±0.07	
J0941+1331	-4874	329	6.8%				0.29±0.12
J1111+1437	-1846	666	1.6%				0.27±0.04
J1135+1615	-6754	1332	4.4%	1.33±0.54			
J1512+1119 A	-1876	335	6.2%		1.00±0.05		
J1512+1119 B	-1053	322	1.8%				0.08±0.09
Total population				1	1	2	4

Note. — Same as Table 4 for the VLT/XShooter sample.

outflows with $0.8 < N(\text{SiIV}^*)/N(\text{SiIV}) < 1.2$. Column 7 and 8 give $N(\text{SiIV}^*)/N(\text{SiIV}) < 0.8$, for which we are certain that $n_e < n_{\text{cr}}$ and therefore $R > 100$ pc (corresponds to the first two rows in Table 1). We further split this category into two columns, where the outflows in column 8 have $N(\text{SiIV}^*)/N(\text{SiIV}) < 0.5$, where no reasonable error can bring the actual ratio to be consistent with $n_e \geq n_{\text{cr}}$.

We find that 53% (18 out of 34) of the outflows have $N(\text{SiIV}^*)/N(\text{SiIV}) < 0.8$, which situates them at distances of more than 100 pc from the central source (see § 2.3). In 14 outflow components, this assertion is more robust, as they have $N(\text{SiIV}^*)/N(\text{SiIV}) < 0.5$.

Some of our SiIV troughs might be false-positive identifications due to the Ly α forest contamination. To address the effect of this issue on our results, we use the Monte Carlo simulation statistical figure of merit (see Table 4). On average, only 3.7% of our Monte Carlo simulations give better template fits than the fit at the exact SiIV expected wavelength. Therefore, we expect only about one of the 34 identified SiIV troughs to be a false detection, on average.

To check the empirical situation, we have done the reverse experiment as well. We attempted to identify SiIV* troughs in the population of objects where we did not identify SiIV troughs, that is objects from the original 191 C IV detections (see § 3.1) that do not appear in Table 2 and figure 3 (166 quasars in total). We use the same identification procedure that was used in § 4.1 to identify SiIV* troughs. First, we identify an SiIV outflow component as a kinematic structure that has a local minimum of $I < 0.7$, and whose width is larger than 500 km s^{-1} ; 32 out of the 166 objects showed such components in their spectra. Several of these 32 quasars produce two and even three such SiIV outflow components, for a total of 43 components. Only one of these 43 components showed a good match for an SiIV* trough:

SDSS J1208+0020, where a good fit can be found for an SiIV* trough with an SF=1 ($\Delta v = 700 \text{ km s}^{-1}$ and maximum $\tau_{AOD}=0.5$). The data do not allow any SiIV trough.

Finding only one false-positive detection testifies for the accuracy of our SiIV trough identification method. Furthermore, finding one false identification in 43 components is in good agreement with the Monte Carlo-based 3.7% chance of false identification discussed in the previous paragraph.

In figure 6 we show the distribution of $N(\text{SiIV}^*)/N(\text{SiIV})$ vs. the outflow velocity and velocity width. We find no correlation of $N(\text{SiIV}^*)/N(\text{SiIV})$ with the outflow's velocity. We do find some correlation between $N(\text{SiIV}^*)/N(\text{SiIV})$ and the velocity width of the outflows, as all four outflows with $\Delta v > 2000 \text{ km s}^{-1}$ are consistent with $N(\text{SiIV}^*)/N(\text{SiIV}) = 1$

5.1.1. Notes for individual outflows

(a)– J1145+2359 is the one case where we used the percentage fit of the SiIV* trough. This was done because the SiIV and SiIV* troughs are so wide that they self-blend, leaving the low velocity of the SiIV* trough as the only clearly identifiable feature while using the SiIV template. (b)– For the outflow J1347+4654A, the ratio $N(\text{SiIV}^*)/N(\text{SiIV}) = 3.2$ is unphysical (as the maximum can only be 2). This high value arises because

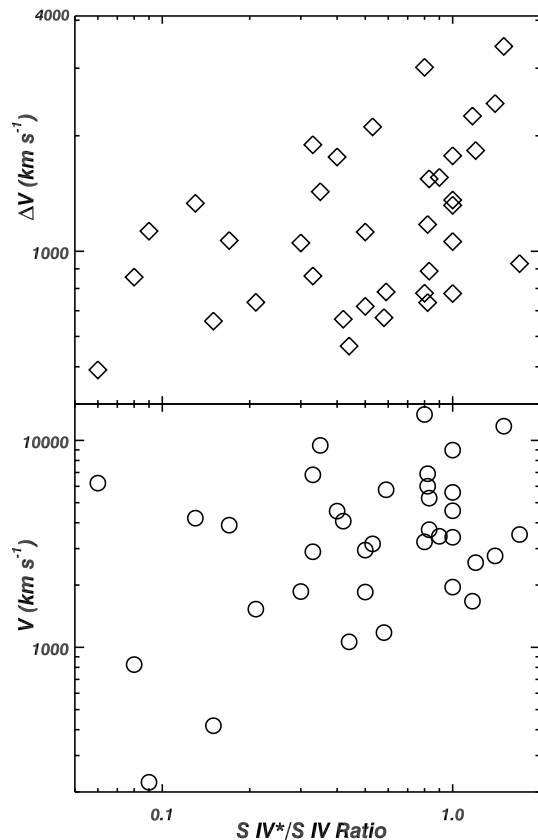


Figure 6. Possible correlations for the SDSS sample. Top panel: Velocity width of the SiIV outflow components as a function of $N(\text{SiIV}^*)/N(\text{SiIV})$. Bottom panel: velocity centroid of the SiIV outflow components as a function of $N(\text{SiIV})/N(\text{SiIV}^*)$. All outflows in Table 4 are shown in both panels.

what is fitted as the SiIV* trough for component A is mostly due to the SiIV trough for component B; see Fig. 3.

(c)– J1407+4037 has the widest BAL in the SiIV sample, with a C IV balnicity of $17,000 \text{ km s}^{-1}$, and it has a deep and very wide blended SiIV/SiIV* BAL (see Fig. 3). The SiIV trough of this wide outflow is the only one in the SiIV sample that does not show distinct components. We did not want to exclude this object from the analysis, as it will bias the sample against the widest BALs. Therefore, we fit the high-velocity portion of the SiIV trough (which is the least-blended portion of the trough) and use it as a template for the SiIV region. The width of the template was chosen to be 2900 km s^{-1} as that is the velocity separation between the SiIV and SiIV* transitions.

5.2. VLT/X-shooter Sample

The VLT/X-shooter data has three times the spectral resolution and two to three times the S/N of the SDSS data. Therefore, we look for SiIV absorption troughs that accompany an SiIV trough wider than 150 km s^{-1} . From the right identified SiIV outflow troughs, four are narrower than 500 km s^{-1} . Seven of these outflows are shown in figure 4 and another outflow (in SDSS J0831+0354) is analyzed and discussed intensively in Chamberlain et al. (2015a)

We find that six (75%) of the right outflows have $N(\text{SiIV}^*)/N(\text{SiIV}) < 1$, which situates them at distances of more than 100 pc from the central source (see § 2.3).

While the sample is small, it suggests that better data resolve some of the ambiguity due to Ly α forest contamination and reveals a higher percentage of outflows with $R > 100$ pc.

5.3. Very Large Scale Outflows

Four of the 34 SDSS/BOSS and one of the right X-shooter outflows have no detected SIV* trough; thus, we can put a conservative upper limit of $N(\text{SIV}^*)/N(\text{SIV}) < 0.1$. These outflows tend to have smaller values of $N(\text{SIV})_{\text{AOD}}$, resulting in lower values of U_H and therefore larger distances for a given $N(\text{SIV}^*)/N(\text{SIV})$. As a result, the $N(\text{SIV}^*)/N(\text{SIV}) < 0.1$ outflows have $R > 1000$ pc. For example, a detailed photoionization solution for component B in SDSS 1512+1119 was published by Borguet et al. (2013), where an upper limit of $N(\text{SIV}^*)/N(\text{SIV}) < 0.1$ was converted to a lower limit of $R > 3300$ pc.

5.4. What Is the R Value for Outflows with $N(\text{SIV}^*)/N(\text{SIV}) \geq 1$?

When $N(\text{SIV}^*)/N(\text{SIV}) \geq 1$, we only have an upper limit on R . Therefore, in principle, R can be as small as the radius of the accretion disk around the supermassive black hole ($R \leq 0.01$ pc). However, there are two empirical observations that suggest larger R values in this case. First, there is one case where $N(\text{SIV}^*)/N(\text{SIV}) \geq 1$ is found, but there exist other high-quality excited-state trough diagnostics that are sensitive to $n_e > n_{\text{cr}}(\text{SIV})$. In that object (SDSS J1512+1119), VLT/X-shooter data show identical SIV 1062.66Å and SIV* 1072.96Å troughs (see Borguet et al. 2012b, Fig. 4). In the same, data we also detect CIII* troughs that allow us to constrain $10^{4.8} \leq n_e \leq 10^{8.1}$ (cm $^{-3}$) (see Borguet et al. 2012b, Fig. 5), which leads to $10 \text{ pc} < R < 300 \text{ pc}$ (Borguet et al. 2013). This excludes wind accelerated from the accretion disk as the origin of that outflow.

A more general argument comes from the similarity of all SIV outflows. The observed velocity and velocity width of the troughs are quite similar for objects with $N(\text{SIV}^*)/N(\text{SIV}) < 1$ ($R > 100$ pc) and objects with $N(\text{SIV}^*)/N(\text{SIV}) \geq 1$. This is evident in figure 6 (where errors in determining v and Δv are less than 100 km s^{-1}). Such characteristics are easier to explain if more of the $N(\text{SIV}^*)/N(\text{SIV}) \geq 1$ outflows have $100 \text{ pc} > R > 10 \text{ pc}$ than $1 \text{ pc} > R > 0.01 \text{ pc}$, as outflows with the latter range of R require much more fine-tuning to look like their relatives at $R > 100$ pc. This is because photoionization arguments require $n_e \propto R^{-2}$ and most acceleration mechanisms tend to yield a higher velocity for outflows originating at smaller R (for example, $v \propto R^{-1/2}$ is typical for radiative acceleration scenarios; (e.g., Arav et al. 1994).

6. EXTRAPOLATING THE SIV RESULTS TO THE GENERAL POPULATION OF HIBAL OUTFLOWS

As described above, we found that half of the SIV outflows found in our survey are situated at distances larger than 100 pc from the central source. Here we detail the steps and assumptions that are needed to extend these results to the general population of HiBAL outflows.

6.1. Extrapolation to all CIV BALs in our sample

In the parent sample of 1091 quasars, we identify 130 CIV absorption components that qualify for the width definition of a BAL (see Weymann et al. 1991). We note that our BAL detection fraction ($130/1091=12\%$) is similar to the detection rate of CIV BALs in optical surveys: e.g., $15 \pm 3\%$ found for the large bright quasar survey between redshifts 1.5 and 3 (Hewett & Foltz 2003) and $10.4 \pm 0.2\%$ in the SDSS DR3 catalog for the redshift range 1.7 – 4.38, (Trump et al. 2006). Therefore, our selection criteria of CIV trough with minimum residual intensity (I) less than 0.5 does not miss a significant population of BALs. However, we note that our results are not applicable to CIV BAL systems with minimal $I > 0.5$.

In 32 of these 130 CIV BALs, which represents 25% of the total BAL outflows, we identified SIV absorption features (see Tables 2 and 4). The first issue is: can the SIV results be extrapolated to the 75% of the CIV BAL outflows in our sample where there is no clear detection of corresponding SIV absorption?

As shown by Dunn et al. (2012), in photoionization equilibrium, the ratio of SIV to CIV ionic column densities is rather constant (to within a factor of 3) as a function of the photoionization parameter (U_H) in the range $-4 < \log(U_H) < -1$. This demonstrates that CIV and SIV are formed in the same physical region of the outflow. However, for solar metallicity, the expected optical depth ratio $\tau(\text{SIV } \lambda 1063)/\tau(\text{CIV } \lambda 1548) \sim 0.01$ for the same span of U_H values. This small ratio is due the lower abundance of sulfur compared to carbon (roughly 1/16 for solar abundances), a ratio of 1/4 in oscillator strengths, and a ratio of 2/3 in wavelength ratio (see Eq. (2) in Dunn et al. 2012).

The small expected τ ratio explains the absence of SIV absorption associated with 75% of the CIV BALs in our sample. For a given U_H value, there is a large range of total hydrogen column density (N_H) that produces a BAL with $\tau(\text{CIV})$ between 0.5 and 30, which is easily detectable. However, since for the same N_H $\tau(\text{SIV})/\tau(\text{CIV}) \sim 0.01$ (see above paragraph), $\tau(\text{SIV})$ is between roughly 0.005 and 0.3, which is undetectable amidst the Ly α forest absorption features, even at the high-end value. Only outflows with larger N_H would produce detectable SIV absorption associated with the same BAL.

Therefore, to extend the SIV results to the 75% of the CIV BAL outflows in our sample where there is no clear detection of corresponding SIV absorption, we need two assumptions.

1) The difference in CIV vs. SIV absorption detection is mainly due to the latter needing a larger N_H to be detected.

We note that the larger N_H needed for the detection of SIV absorption also explains the higher fraction of observed SiIV and AlIII in these outflows.

2) Outflows with lower N_H (where it is difficult to detect SIV absorption troughs) are not preferentially found at smaller distances than outflows with higher N_H .

To address this issue, we examine the relationship between R and N_H for outflows where R was determined using doubly and triply ionized species (see discussion in the Introduction). Table 6 shows the published parameters of these outflows. The trend is for lower N_H outflows to be found at larger R than outflows with higher N_H .

Table 6
Outflows with Published Distances Based on High-ionization Diagnostics.

Object (1)	Distance Diagnostic	$\log(N_H)$ (cm^{-2})	R (pc)	<i>Ref</i>
SDSS J0831+0354	S IV	22.5	110	1
SDSS J1106+1939	S IV	22.1	320	2
SDSS J1512+1119A	S IV and C III	21.9	10-300	2
SDSS J1111+1437	S IV	21.5	880	3
HE0238-1904	O IV	20.7	1700	4
SDSS J1206+1052	N III and S III	20.5	840	5
SDSS J1512+1119B	S IV	20.1	>3000	2
FBQS J0209-0438	O IV	20.0	4000	6

Note. — References 1: Chamberlain et al. (2015a); 2: Borguet et al. (2013); 3: Xu et al. (2018); 4: Arav et al. (2013); 5: Chamberlain & Arav (2015b); 6: Finn et al. (2014).

We also note that with high-quality data, it is possible to detect S IV outflows with lower N_H . The one example we have is SDSS J1512+1119B (based on VLT/X-shooter data), which has the second-lowest N_H in Table 6 and the second-largest R . We conclude that the data at hand do not support the possibility that outflows with lower N_H are found preferentially at smaller R than outflows with higher N_H .

6.2. Extending the Results to Fainter and Lower-Redshift Objects

Due to instrument and S/N considerations, our parent sample of 1091 objects is limited to a redshift above 2.6 and an r magnitude larger than 18.5. Extrapolating the S IV results to lower redshift and fainter objects implicitly assumes that the physical nature of the outflows does not depend strongly on the redshift or brightness of the observed objects. To date, we are unaware of published results suggesting that the physical nature of BAL outflows depends on the brightness or redshift of the observed quasar.

7. DISCUSSION

7.1. Comparison of Distance Determination Methods for AGN Outflows

In this paper, we concentrated on the excited-state trough method for finding the distance of the outflow from the central source (R). In the literature, we find four other methods for deducing R . Here we describe these methods and compare their advantages and disadvantages to those of the excited-state trough method.

(1) The most robust method for R determination uses spatially resolved spectroscopy (usually integral field unit spectroscopy (IFU)) to directly measure the size of the outflow across the field of view. This method is used extensively in the study of Seyfert outflows (e.g. Barbosa et al. 2009; Riffel & Storchi-Bergmann 2011), as well as for outflows in luminous quasars (e.g., Liu et al. 2013a,b, 2014, 2015; Cano-Díaz et al. 2012; Harrison et al. 2012, 2014; McElroy et al. 2015). A typical spatial resolution of $\geq 0.5''$ limits this method to large-scale outflows: a few tens of pc in nearby AGNs and several thousand pc for luminous quasars at redshifts larger than ~ 0.5 . Such outflows are readily observed with these IFU observations. For luminous quasars, typical

outflow values are $R \sim 15,000$ pc and $v \lesssim 1000$ km s $^{-1}$. The drawback of this method is its current inability to probe luminous quasar outflows on scales of less than several thousand pc for luminous quasars at redshifts larger than 0.5, even using adaptive optics. Observing larger-scale outflows using IFU data does not exclude the possibility of outflows on much smaller R values.

Two other methods use trough variability. The idea is to translate the time-scale of variability seen in the outflow troughs (e.g. Barlow et al. 1992; Filiz Ak et al. 2013; Grier et al. 2016; Rogerson et al. 2016; Matthews et al. 2016) into constraints on R . These efforts are dependent on the mechanism assumed to cause the trough’s variability. There are two main mechanisms invoked to explain trough variability.

(2) Changes in the ionizing flux incident on the outflow alter the ionization equilibrium, which increases or decreases the fractional abundance of a given ion. Such an occurrence does not necessitate a change in the total column density of the absorber. Since photoionization changes are a time-dependent process, the time-scale for variability (or lack thereof) can be used to extract constraints on the electron number density (n_e ; e.g., Krolik & Kriss 2001; Arav et al. 2012, 2015). These n_e constraints, combined with a photoionization solution for the outflow, yield constraints on R (similar to the method described in § 2.3). Uncertainties on the ionizing flux light curve, as well as decreasing variability on smaller timescales, causes this method to be less reliable than the excited-state trough method.

(3) Trough changes are attributed to material crossing the line of sight. With an estimate of the emission region’s size and assuming a Keplerian-dominated tangential motion for the absorbing material, it is possible to constrain R using the variability time-scale of the trough (e.g., Moe et al. 2009; Capellupo et al. 2011, 2012). In general, such an occurrence requires a change in the total column density of the absorber. The assumption of Keplerian-dominated tangential motion and the lack of a self-consistent model for the changes in the troughs’ depth cause this method to be less reliable than the excited-state trough method (see § 2).

Unfortunately, the two mechanisms invoked to explain trough variability provide very different R estimates; therefore, unless we can ascertain the underlying mechanism for trough variability, it is impossible to deduce robust constraints on R from studying trough variability. The best-studied case of AGN trough variability is from two monitoring campaigns of NGC 5548, where many simultaneous determinations of UV trough shapes, the UV broadband flux curve, and X-ray flux are available (see Kaastra et al. 2014; Peterson et al. 2014). For this case, the changes in the ionizing flux model yield R estimates fully consistent with the excited-state trough method (Arav et al. 2015), while the material crossing the line-of-sight model is inconsistent with the R derived from the excited-state trough method.

For BAL outflows, recent analysis suggests that variation of the ionizing continuum is the main driver of most observed BAL variability (He et al. 2017). Two published analyses of individual objects that attempt to decide the variability mechanism support a different interpretation in each case: Capellupo et al. (2014) argued for the material crossing the line-of-sight explanation,

while Stern et al. (2017) supported the changes in the ionizing flux mechanism.

(4) When the data do not include any possible R diagnostics, some works simply assume an R value. The common procedure is to assume a distance where the measured radial velocity (v) equals the escape velocity from the supermassive black hole (SMBH): $R = 2GM/v^2$, where M is the mass of the SMBH and G is the constant of gravity. This method is popular with the claimed detection of ultra-fast outflows (UFO) in X-ray data (e.g., Tombesi et al. 2011).

From the discussion above, we conclude that the excited-state trough method is the most reliable and model-independent R determination method for quasar absorption outflows. It is also the only method that can currently probe outflows with R smaller than a few thousand pc for quasars at redshifts larger than 0.5.

7.2. Avoiding Selection Biases When Using the SIV/SIV* R Determination Method

Lucy et al. (2014) criticized the SIV/SIV* R determination method as suffering from a selection bias, claiming that it cannot be generalized to the whole population of quasar absorption outflows. They pointed correctly to the fact that, given the critical density for the SIV/SIV* energy levels and the finite quality of observed spectra, there is only a certain range of n_e values that can be uniquely determined from the ratio $N(\text{SIV}^*)/N(\text{SIV})$. Their given range, $4.5 \times 10^2 \text{ cm}^{-3} < n_e < 1.7 \times 10^5 \text{ cm}^{-3}$, will allow a unique distance determination for the range $50 \text{ pc} \lesssim R \lesssim 2000 \text{ pc}$ (see §2.3 here). This in turn will cause a bias toward R values in the range 50–2000 pc, as an accurate n_e cannot be measured by the ratio $N(\text{SIV}^*)/N(\text{SIV})$ for $n_e > 1.7 \times 10^5 \text{ cm}^{-3}$.

The logical fault with the above argument is that there is important information regarding R even outside the measurable range of n_e values. As we detail in this paper, when $N(\text{SIV}^*)_{\text{AOD}}/N(\text{SIV})_{\text{AOD}} \gtrsim 1$ we can ascertain only a lower limit for n_e and therefore an upper limit of $R \lesssim 100 \text{ pc}$. Similarly, when $N(\text{SIV}^*)_{\text{AOD}}/N(\text{SIV})_{\text{AOD}} < 1$ we can ascertain an upper limit for n_e and therefore a lower limit of $R \gtrsim 100 \text{ pc}$. As mentioned above, if the large majority of quasar outflows were situated at $R < 1 \text{ pc}$, then in the large majority of cases, we would have found $N(\text{SIV}^*)_{\text{AOD}}/N(\text{SIV})_{\text{AOD}} \gtrsim 1$. Our SIV surveys show that this is not the case: roughly 50% of SIV outflows have $N(\text{SIV}^*)_{\text{AOD}}/N(\text{SIV})_{\text{AOD}} < 1$ and are therefore at $R > 100 \text{ pc}$.

Our methodology specifically avoids a bias toward a certain range of $N(\text{SIV}^*)/N(\text{SIV})$ values. We do so by concentrating on identifying an SIV outflow trough and only then establishing whether an associated SIV* outflow trough exists and at what depth.

7.3. Implication tfor AGN Wind Models

Theoretical studies of AGN wind models have a long history. The best-studied models use the AGN accretion disk as the source of the wind and accelerate the material with radiation pressure using the central source’s luminosity (e.g. Murray et al. 1995; Proga et al. 2000; Proga & Kallman 2004). The width of the absorption troughs is attributed to the acceleration phase of the

Table 7
Electron Temperature in Kelvin
averaged over the SIV region.

Z	SED	$\log U_{\text{H}}$			
		-2	-1	0	1
1Z _⊙	MF87	11,000	11,000	12,000	13,000
1Z _⊙	HE0238	9600	9800	10,000	11,000
1Z _⊙	UVSoft	11,000	11,000	11,000	12,000
1Z _⊙	NGC 5548	13,000	12,000	12,000	12,000
4Z _⊙	MF87	6600	6800	7400	7800
4Z _⊙	HE0238	6100	6200	6500	7100
4Z _⊙	UVSoft	7000	6400	6800	7200
4Z _⊙	NGC 5548	8000	7300	7600	7900

Note. — SED references:

- For MF87, HE0238, and HE0238, see Arav et al. (2013), Figure 10 and Table 2.

- For NGC5548, see Steenbrugge et al. (2005), Figure 1.

winds seen along our line of sight. In such models for luminous quasars, most of the acceleration is done within several times 10^{16} cm ($\sim 0.01 \text{ pc}$) from the central source (e.g. Higginbottom et al. 2014, Figure 1). Clearly, these accretion disk wind models are hard-pressed to explain absorption outflows situated at 100 pc or more from the central source.

A different set of AGN wind models pertains to lower-luminosity AGNs and attempts to explain their UV troughs and warm absorbers (the X-ray absorption manifestation of the wind). In some of these models, the source of the outflowing matter is photoionized evaporation from the inner edge of the obscuring torus often found surrounding an AGN (e.g., Krolik & Kriss 2001). Other models invoke magnetohydrodynamic (MHD) wind from a clumpy molecular accretion disk to explain observations of warm absorbing gas at UV and X-ray energies in Seyfert 1 galaxies (e.g. Bortorff et al. 2000). Both models create the wind at $R \sim 1 - 10 \text{ pc}$, with wind velocities up to $\sim 1000 \text{ km s}^{-1}$. The applicability of these models to faster outflows ($\sim 10,000 \text{ km s}^{-1}$) in luminous quasars is not well explored in the literature.

A different kind of model creates the observed absorption troughs “in situ in radiative shocks produced when a quasar blast wave impacts a moderately dense interstellar clump along the line of sight” at hundreds or thousands of parsecs from the central source (Faucher-Giguère et al. 2012). This model is designed to explain the type of winds we empirically detect on such scales.

7.4. The effect of finite Temperature

Equation (1) shows that in the high- n_e limit, the maximum ratio of $N(\text{SIV}^*)/N(\text{SIV}) = 2e^{-\Delta E/kT}$. For SIV, $e^{-\Delta E/kT} = 0.8$ at 6000 K, so at n_{cr} , $N(\text{SIV}^*)/N(\text{SIV}) = 0.8$.

Our results in Tables 4 and 5 posit that we treat an outflow as having $N(\text{SIV}^*)/N(\text{SIV}) < 1$ only if the actual ratio is less than 0.8. Therefore, it is important to verify that for plasma photoionized by a quasar spectrum, the region where SIV exists has $T > 6000 \text{ K}$. We used our grid of photoionization models to find the temperature in the SIV zone. We checked the range of $0.01 < U_{\text{H}} < 10$, which extends more than an order of magnitude on ei-

ther side of the U_{H} solutions for published photoionization analysis of SIV outflows (Borguet et al. 2012b, 2013; Chamberlain et al. 2015a). We did so for three Spectral Energy Distributions (SED) used for quasar outflow studies in the literature and one Seyfert SED. A range of metallicity is $1 < Z < 4$, where $Z = 4$ solar was chosen as the upper limit, since Borguet et al. (2012b) showed that it is already too high a metallicity value for an SIV outflow. Table 7 shows the temperature over the SIV region for the four SED, at four U_{H} values and the chosen metallicity boundaries. In all cases, $T > 6000$ K, thus, our analysis is robust for realistic cases of a quasar-photoionized SIV absorber.

8. SUMMARY

In quasar outflow research, arguably the most important question is: what is the distance of the outflows from the central source? Most of the fundamental issues in this field are directly tied to the distribution of R values:

- the origin and acceleration mechanism of the outflows.
- the influence of the outflow on the formation and evolution of the host galaxy, since the mass, momentum, and kinetic energy fluxes of the outflow depend linearly on R (e.g. Borguet et al. 2012a).
- the relationship between mass accretion and mass ejection from the environment of the black hole, since the mass flux of the outflow depends linearly on R .

Over the past 15 yr, roughly 20 individual observational studies using excited-state troughs found $10 \text{ pc} \lesssim R \lesssim 10,000 \text{ pc}$, while many theoretical works put the outflows at $R \sim 0.01 \text{ pc}$ (see § 1). The 20 outflows for which R was determined suffered from selection effects (see § 1), which did not allow for a simple extrapolation of the results to the majority of quasar outflows.

To overcome these biases, in this paper, we executed the following program:

1. We targeted the SIV ion. The fractional abundances of SIV and CIV peak at similar values of the ionization parameter, implying that they arise from the same physical component of the outflow (see Section 3 and Fig. 3 in Dunn et al. 2012). Therefore (as discussed in § 1), the SIV troughs give the best distance proxy for the majority of quasar outflows that show CIV troughs.
2. In § 2, we demonstrated that the AOD ratio of the SIV* and SIV trough provides robust information about R , even while taking into account non-black saturation that is common in quasar outflow troughs.
3. We then chose two unbiased quasar samples for our SIV survey. The first sample included the 1091 brightest SDSS and BOSS quasar spectra, where the spectral regions of possible SIV and SIV* outflow troughs are covered (see § 3.1). The second sample was a blind sample of 13 bright SDSS and

BOSS quasars, where the spectral regions of possible SIV and SIV* outflow troughs were not covered by the SDSS and BOSS data. We then observed these quasars using VLT/X-shooter, whose short-wavelength coverage allowed us to observe the spectral region of the SIV and SIV* outflow troughs. These observations have much higher spectral resolution and S/N compared to the SDSS and BOSS observations.

4. In § 4 we identified all the robust cases of SIV outflow trough detections and searched for SIV* outflow troughs associated with the same outflow component. We then ran Monte Carlo simulations to quantitatively assess the reliability of the SIV trough detection.
5. Following the methodology described in § 2 and 3, we separated the SIV outflows into different distance groups (Tables 4 and 5). These results are summarized in Table 8.

Results (see Table 8): In each of the samples we analyze, we find that at least 50% of quasar outflows have R larger than 100-200 pc, and at least 12% are at distances larger than 1000 pc. Higher-quality data hint that a greater fraction (3/4) of the outflows have R larger than 100-200 pc, but our sample size of the VLT/X-shooter outflows is too small (eight outflows) to derive statistically meaningful results. These R values have profound implications for the study of the origin and acceleration mechanism of quasar outflows and their effects on the host galaxy.

NA acknowledges support from NSF grant AST 1413319, as well as NASA STScI grants GO 14242, 14054, and 14176, and NASA ADAP 48020.

Based on observations collected at the European Organisation for Astronomical Research in the Southern Hemisphere under ESO programs, 091.B-0324, 092.B-0267, 091.B-0324, 091.B-0324, and 090.B-0424.

Funding for SDSS-III has been provided by the Alfred P. Sloan Foundation, the Participating Institutions, the National Science Foundation, and the U.S. Department of Energy Office of Science. The SDSS-III website is <http://www.sdss3.org/>.

SDSS-III is managed by the Astrophysical Research Consortium for the Participating Institutions of the SDSS-III Collaboration, including the University of Arizona, the Brazilian Participation Group, Brookhaven National Laboratory, Carnegie Mellon University, the University of Florida, the French Participation Group, the German Participation Group, Harvard University, the Instituto de Astrofísica de Canarias, the Michigan State/Notre Dame/JINA Participation Group, Johns Hopkins University, Lawrence Berkeley National Laboratory, the Max Planck Institute for Astrophysics, the Max Planck Institute for Extraterrestrial Physics, New Mexico State University, New York University, Ohio State University, Pennsylvania State University, the University of Portsmouth, Princeton University, the Spanish Participation Group, the University of Tokyo, the University of Utah, Vanderbilt University, the University of Virginia, the University of Washington, and Yale University.

Table 8
Distance from the central source based on an observed S IV 1062Å Trough,
and number of outflows in each category

S IV* 1073Å Trough	n_e	R (pc)	SDSS	VLT
Undetected	$n_e < n_{\text{AOD}} < n_{\text{cr}}$	$R > 1000$	4	1
Shallower than S IV	$n_{\text{PI}} < n_e < n_{\text{AOD}} < n_{\text{cr}}$	$R_{n_{\text{PI}}} > R > 100$	14	5
Similar depth to S IV	$n_{\text{PI}} < n_e$	$R < R_{n_{\text{PI}}}$	12	1
Deeper than S IV	$n_{\text{cr}} < n_{\text{AOD}} < n_e$	$R < 100$	4	1

Note. — Definitions: n_e , electron number density; n_{AOD} , value of n_e determined from the ratio $N(\text{S IV}^*)_{\text{AOD}}/N(\text{S IV})_{\text{AOD}}$ (see Fig. 1); n_{cr} , critical density of the S IV/S IV* energy levels, $n_{\text{cr}} = 5.6 \times 10^4 \text{ cm}^{-3}$ at 10,000 K; n_{PI} , lower limit on n_e from photoionization modeling that give the upper limit to $N(\text{S IV})$; and $R_{n_{\text{PI}}}$, the distance of the outflow when $n_e = n_{\text{PI}}$, illustrated by the left boundary of the blue and green zones in Fig. 2. (For elaboration on these quantities, see § 2.2 and 2.3.)

GL is supported by the National Thousand Young Talents Program of China and acknowledges the grant from the National Natural Science Foundation of China (No. 11673020 and No. 11421303) and the Ministry of Science and Technology of China (National Key Program for Science and Technology Research and Development, No. 2016YFA0400700).

Facilities: VLT SDSS.

REFERENCES

- Alam, S., Albareti, F. D., Allende Prieto, C., et al. 2015, *ApJS*, 219, 12
- Aoki, K., Oyabu, S., Dunn, J. P., et al. 2011, *PASJ*, 63, 457
- Arav, N., Li, Z.-Y., & Begelman, M. C. 1994, *ApJ*, 432, 62
- Arav, N. 1997, *Mass Ejection from Active Galactic Nuclei*, ASP Conference Series; Vol. 128, p.208
- Arav, N., Korista, K. T., de Kool, M., Junkkarinen, V. T., & Begelman, M. C. 1999, *ApJ*, 516, 27
- Arav, N., de Kool, M., Korista, K. T., et al. 2001, *ApJ*, 561, 118
- Arav, N., Kaastra, J., Steenbrugge, K., et al. 2003, *ApJ*, 590, 174
- Arav, N., Kaastra, J., Kriss, G. A., et al. 2005, *ApJ*, 620, 665
- Arav, N., Moe, M., Costantini, E., et al. 2008, *ApJ*, 681, 954
- Arav, N., Edmonds, D., Borguet, B., et al. 2012, *A&A*, 544, AA33
- Arav, N., Borguet, B., Chamberlain, C., Edmonds, D., & Danforth, C. 2013, *MNRAS*, 436, 3286
- Arav, N., Chamberlain, C., Kriss, G. A., et al. 2015, *A&A*, 577, A37
- Barbosa, F. K. B., Storch-Bergmann, T., Cid Fernandes, R., Winge, C., & Schmitt, H. 2009, *MNRAS*, 396, 2
- Barlow, T. A., Junkkarinen, V. T., Burbidge, E. M., et al. 1992, *ApJ*, 397, 81
- Bautista, M. A., Dunn, J. P., Arav, N., et al. 2010, *ApJ*, 713, 25
- Borguet, B. C. J., Edmonds, D., Arav, N., Dunn, J., & Kriss, G. A. 2012a, *ApJ*, 751, 107
- Borguet, B. C. J., Edmonds, D., Arav, N., Benn, C., & Chamberlain, C. 2012, *ApJ*, 758, 69
- Borguet, B. C. J., Arav, N., Edmonds, D., Chamberlain, C., & Benn, C. 2013, *ApJ*, 762, 49
- Bottoff, M. C., Korista, K. T., & Shlosman, I. 2000, *ApJ*, 537, 134
- Cano-Díaz, M., Maiolino, R., Marconi, A., et al. 2012, *A&A*, 537, LL8
- Capellupo, D. M., Hamann, F., Shields, J. C., Rodríguez Hidalgo, P., & Barlow, T. A. 2011, *MNRAS*, 413, 908
- Capellupo, D. M., Hamann, F., Shields, J. C., Rodríguez Hidalgo, P., & Barlow, T. A. 2012, *MNRAS*, 422, 3249
- Capellupo, D. M., Hamann, F., & Barlow, T. A. 2014, *MNRAS*, 444, 1893
- Chamberlain, R. T., Dalal, N., Hearin, A., & Ricker, P. 2015, *MNRAS*, 451, 1496
- Chamberlain, C., & Arav, N. 2015, *MNRAS*, 454, 675
- Choi, E., Naab, T., Ostriker, J. P., Johansson, P. H., & Moster, B. P. 2014, *MNRAS*, 442, 440
- Ciotti, L., Ostriker, J. P., & Proga, D. 2010, *ApJ*, 717, 708
- Dai, X., Shankar, F., & Sivakoff, G. R. 2008, *ApJ*, 672, 108
- Dai, X., Shankar, F., & Sivakoff, G. R. 2012, *ApJ*, 757, 180
- de Kool, M., Arav, N., Becker, R. H., et al. 2001, *ApJ*, 548, 609
- de Kool, M., Becker, R. H., Gregg, M. D., White, R. L., & Arav, N. 2002, *ApJ*, 567, 58
- de Kool, M., Korista, K. T., & Arav, N. 2002, *ApJ*, 580, 54
- Del Zanna, G., Dere, K. P., Young, P. R., Landi, E., & Mason, H. E. 2015, *A&A*, 582, A56
- Dere, K. P., Landi, E., Mason, H. E., Monsignori Fossi, B. C., & Young, P. R. 1997, *A&AS*, 125, 149
- Dunn, J. P., Bautista, M., Arav, N., et al. 2010, *ApJ*, 709, 611
- Dunn, J. P., Arav, N., Aoki, K., et al. 2012, *ApJ*, 750, 143
- Edmonds, D., Borguet, B., Arav, N., et al. 2011, *ApJ*, 739, 7
- Elvis, M. 2000, *ApJ*, 545, 63
- Faucher-Giguère, C.-A., Quataert, E., & Murray, N. 2012, *MNRAS*, 420, 1347
- Filiz Ak, N., Brandt, W. N., Hall, P. B., et al. 2013, *ApJ*, 777, 168
- Finn, C. W., Morris, S. L., Crighton, N. H. M., et al. 2014, *MNRAS*, 440, 3317
- Gabel, J. R., Kraemer, S. B., Crenshaw, D. M., et al. 2005, *ApJ*, 631, 741
- Ganguly, R., & Brotherton, M. S. 2008, *ApJ*, 672, 102
- Grier, C. J., Brandt, W. N., Hall, P. B., et al. 2016, *ApJ*, 824, 130
- Harrison, C. M., Alexander, D. M., Swinbank, A. M., et al. 2012, *MNRAS*, 426, 1073
- Harrison, C. M., Alexander, D. M., Mullaney, J. R., & Swinbank, A. M. 2014, *MNRAS*, 441, 3306
- Hamann, F. W., Barlow, T. A., Chaffee, F. C., Foltz, C. B., & Weymann, R. J. 2001, *ApJ*, 550, 142
- Hamann, F., & Sabra, B. 2004, *AGN Physics with the Sloan Digital Sky Survey*, 311, 203
- Hamann, F., Chartas, G., McGraw, S., et al. 2013, *MNRAS*, 435, 133
- He, Z., Wang, T., Zhou, H., et al. 2017, *ApJS*, 229, 22
- Hewett, P. & Foltz, C. 2003, *AJ*, 125, 1784
- Higginbottom, N., Proga, D., Knigge, C., et al. 2014, *ApJ*, 789, 19
- Hopkins, P. F., & Elvis, M. 2010, *MNRAS*, 401, 7
- Kaastra, J. S., Ebrero, J., Arav, N., et al. 2014, *A&A*, 570, A73
- Knigge, C., Scaringi, S., Goad, M. R., & Cottis, C. E. 2008, *MNRAS*, 386, 1426
- Krolik, J. H., & Kriss, G. A. 2001, *ApJ*, 561, 684
- Leighly, K. M., Hamann, F., Casebeer, D. A., & Grupe, D. 2009, *ApJ*, 701, 176
- Liu, G., Zakamska, N. L., Greene, J. E., Nesvadba, N. P. H., & Liu, X. 2013a, *MNRAS*, 430, 2327
- Liu, G., Zakamska, N. L., Greene, J. E., Nesvadba, N. P. H., & Liu, X. 2013b, *MNRAS*, 436, 2576
- Liu, G., Zakamska, N. L., & Greene, J. E. 2014, *MNRAS*, 442, 1303
- Liu, G., Arav, N., & Rupke, D. S. N. 2015, *ApJS*, 221, 9
- Lucy, A. B., Leighly, K. M., Terndrup, D. M., Dietrich, M., & Gallagher, S. C. 2014, *ApJ*, 783, 58
- Luo, B., Brandt, W. N., Alexander, D. M., et al. 2014, *ApJ*, 794, 70
- Matthews, J. H., Knigge, C., Long, K. S., et al. 2016, *MNRAS*, 458, 293
- McCarthy, I. G. et al. 2010, *MNRAS*, 406, 822
- McElroy, R., Croom, S. M., Pracy, M., et al. 2015, *MNRAS*, 446, 2186
- Moe, M., et al. 2009, *ApJ*, 706, 525
- Murray, N., Chiang, J., Grossman, S. A., & Voit, G. M. 1995, *ApJ*, 451, 498

- Osterbrock, D. E., & Ferland, G. J. 2006, *Astrophysics of Gaseous Nebulae and Active Galactic Nuclei* (2nd. ed.; Sausalito, CA: Univ. Science Books)
- Ostriker, J. P., Choi, E., Ciotti, L., Novak, G. S., & Proga, D. 2010, *ApJ*, 722, 642
- Pâris, I., Petitjean, P., Ross, N. P., et al. 2017, *A&A*, 597, A79
- Peterson, B. M., Grier, C. J., Horne, K., et al. 2014, *ApJ*, 795, 149
- Proga, D., Stone, J. M., & Kallman, T. R. 2000, *ApJ*, 543, 686
- Proga, D., & Kallman, T. R. 2004, *ApJ*, 616, 688
- Riffel, R. A., & Storchi-Bergmann, T. 2011, *MNRAS*, 417, 2752
- Rogerson, J. A., Hall, P. B., Rodríguez Hidalgo, P., et al. 2016, *MNRAS*, 457, 405
- Schneider, D. P., Richards, G. T., Hall, P. B., et al. 2010, *AJ*, 139, 2360
- Soker, N. 2010, *MNRAS*, 407, 2355
- Steenbrugge, K. C., Kaastra, J. S., Crenshaw, D. M., et al. 2005, *A&A*, 434, 569
- Stern, D., Graham, M. J., Arav, N., et al. 2017, *ApJ*, 839, 106
- Tombesi, F., Cappi, M., Reeves, J. N., et al. 2011, *ApJ*, 742, 44
- Trump, J. R., Hall, P. B., Reichard, T. A., et al. 2006, *ApJS*, 165, 1
- Verner D. A., Verner E. M., Ferland G. J., 1996, *Atomic Data and Nuclear Data Tables*, 64, 1
- Weymann, R. J., Carswell, R. F., & Smith, M. G. 1981, *ARA&A*, 19, 41
- Weymann, R. J., Morris, S. L., Foltz, C. B., & Hewett, P. C. 1991, *ApJ*, 373, 23